An integrated resource for functional and structural connectivity of the marmoset brain

Xiaoguang Tian[1,*], Yuyan Chen[2], Piotr Majka[3,7], Diego Szczupak[1], Yonatan Sanz Perl[4,11], Cecil Chern-Chyi Yen[5], Chuanjun Tong[2], Kun Song[2], Haiteng Jiang[12,13], Daniel Glen[6], Gustavo Deco[4,8,9,10], Marcello G. P. Rosa[7,*], Afonso C. Silva[1,*], Zhifeng Liang[2,14,15,*], Cirong Liu[2,14,15,*]

[1] Department of Neurobiology, University of Pittsburgh Brain Institute, University of Pittsburgh, Pittsburgh PA 15261, USA
[2] Center for Excellence in Brain Science and Intelligence Technology, Institute of Neuroscience, CAS Key Laboratory of Primate Neurobiology, Chinese Academy of Sciences, Shanghai, China
[3] Laboratory of Neuroinformatics, Nencki Institute of Experimental Biology of the Polish Academy of Sciences, 02-093 Warsaw, Poland
[4] Center for Brain and Cognition, Computational Neuroscience Group, Department of Information and Communication Technologies, Universitat Pompeu Fabra, Roc Boronat 138, Barcelona, 08018, Spain
[5] Cerebral Microcirculation Section, Laboratory of Functional and Molecular Imaging, National Institute of Neurological Disorders and Stroke, National Institutes of Health (NINDS/NIH), Bethesda MD 20892, USA
[6] Scientific and Statistical Computing Core, National Institute of Mental Health, National Institutes of Health (NIMH/NIH), Bethesda MD 20892, USA
[7] Department of Physiology and Neuroscience Program, Biomedicine Discovery Institute, Monash University, Clayton, VIC 3800, Australia
[8] Institució Catalana de la Recerca i Estudis Avançats (ICREA), Passeig Lluís Companys 23, Barcelona, 08010, Spain
[9] Department of Neuropsychology, Max Planck Institute for Human Cognitive and Brain Sciences, 04103 Leipzig, Germany
[10] School of Psychological Sciences, Monash University, Melbourne, Clayton VIC 3800, Australia
[11] Universidad de San Andrés, Vito Dumas 284 (B1644BID), Buenos Aires, Argentina
[12] Department of Neurobiology, Affiliated Mental Health Center & Hangzhou Seventh People's Hospital, Zhejiang University School of Medicine
[13] MOE Frontier Science Center for Brain Science and Brain-machine Integration, Zhejiang University, Hangzhou, China.
[14] University of Chinese Academy of Sciences, Beijing, China
[15] Shanghai Center for Brain Science and Brain-Inspired Intelligence Technology, Shanghai, China
* Corresponding authors

Abstract

Comprehensive integration of structural and functional connectivity data is required for the accurate modeling of brain functions. While resources for studying structural connectivity of non-human primate brains already exist, their integration with functional connectivity data has remained unavailable. Here we present a comprehensive resource that integrates the largest awake non-human primate resting-state fMRI available to date (39 marmoset monkeys, 710 runs, 12117 mins) with previously published cellular-level neuronal tracing (52 marmoset monkeys, 143 injections), and multi-resolution diffusion MRI datasets. The combination of these data allowed us to: (1) map the fine-detailed functional brain networks and cortical parcellations; (2) develop a deep-learning-based parcellation generator that preserves the topographical organization of functional connectivity and reflect individual variabilities, and (3) investigate the structural basis underlying functional connectivity by computational modeling. This resource will enable modeling structure-function relationships and facilitate future comparative and translational studies of primate brains.

Keywords: Resting-state fMRI, non-human primates, functional brain parcellation, computational model, neuronal tracing

Mapping brain architecture is critical for decoding brain functions and understanding the mechanisms of brain diseases [1]. Non-human primate (NHP) neuroimaging provides a granular view of the evolution of the brain [2] and could overcome constraints of human neuroimaging by integration with "ground truth" data from cellular-resolution tracing [3].

As one of the few non-invasive imaging techniques capable of mapping whole-brain functional activity patterns, resting-state fMRI (rs-fMRI) provides insights into large-scale functional architecture [4]. However, data-sharing initiatives of NHP neuroimaging are still at an early stage, with existing open datasets of rs-fMRI data originating in different laboratories and collected for different purposes [5]. This leads to inconsistent imaging protocols and data quality, which hinder analyses across datasets. In addition, most presently available rs-fMRI datasets have been acquired in anesthetized animals, resulting in difficulties for cross-species studies, particularly relative to awake human brains [6]. The final barrier is the practical difficulty of training large numbers of NHPs to be fully awake during MRI scans [7, 8]. Given that, a platform for international collaborative research (PRIMatE RESOURCE EXCHANGE) was initiated to promote open resource exchange and standards for NHP neuroimaging [5, 9].

The common marmoset monkey (*Callithrix jacchus*) has drawn considerable interest as an NHP species, offering many practical advantages for neuroscience research, including neuroimaging [10, 11, 12]. Previous work from our groups has contributed ultra-high-resolution *ex-vivo* diffusion MRI data [13], mesoscale neural tracing data [14], and structural atlases [15, 16, 17], which have enabled an unprecedented level of precision in analyses of NHP brain anatomy. However, an essential component for understanding brain architecture has been missing: integrating these anatomical datasets with rs-fMRI. To address this limitation, and in alignment with a strategic plan developed by the NHP imaging community [8], we developed standardized awake imaging protocols for NHP marmoset monkeys, which were adopted across two institutions, the National Institutes of Health (NIH), USA, and the Institute of Neuroscience (ION), China. This resulted in the largest awake NHP rs-fMRI dataset to date, which is being made available through an open-access platform. Furthermore, we integrated neuronal-tracing and different diffusion MRI

datasets into the same MRI space, resulting in the comprehensive resource which allows us to explore the relationships between the structural and functional connectomes by computational modeling.

Results

The resource reported in this paper (summary in Fig. 1) is underpinned by a publicly available standardized dataset. Following the same protocols for animal training and MRI imaging, including the designs of the radiofrequency coil and MRI pulse sequences, we acquired an extensive awake resting-state fMRI dataset to date from 39 marmosets of two research institutes (13 from ION, age 3+/-1 years old; 26 from NIH, age 4+/-2 years old; 12117 mins in total scanning, Supplementary Table 1 for details). This is also the same range of ages used in our previous studies of structural connectivity [13, 14]. For test-retest evaluation, we scanned multiple runs (17 mins/run) for each marmoset, resulting in an essentially similar data quantity of two institutes (346 ION runs and 364 NIH runs) and included two "flagship" marmosets with many runs (64 runs from the ION and 40 runs from the NIH). Besides similar quantity, we also calculated comprehensive quality measurements (tSNR, CNR, and head motions) to demonstrate the consistency of the data quality from two sites, enabling interpretability across datasets (Supplementary Fig. S1-S3).

Based on these datasets, we created a comprehensive mapping of resting-state brain networks and a fine-grained cortical parcellation based on resting-state functional connectivity. Furthermore, we developed a deep-learning-based approach to map the functional cortical parcellation onto individual brains accurately. This allowed investigation of the structural basis underlying functional connectivity. For this purpose, we sampled the most extensive collection of NHP neuronal tracing data available (52 marmosets and 143 injections) onto the same MRI space at the voxel or vertex level and integrated it with the same functional MRI data space mentioned above. In addition, further enhancing the capacity of our resource, we also integrated extra high-resolution *ex-vivo* diffusion MRI

and *in-vivo* diffusion MRI data obtained at 25 marmosets from the same cohort. On this basis, we investigated the relationship between structural and functional connectivity using a whole-brain computational model.

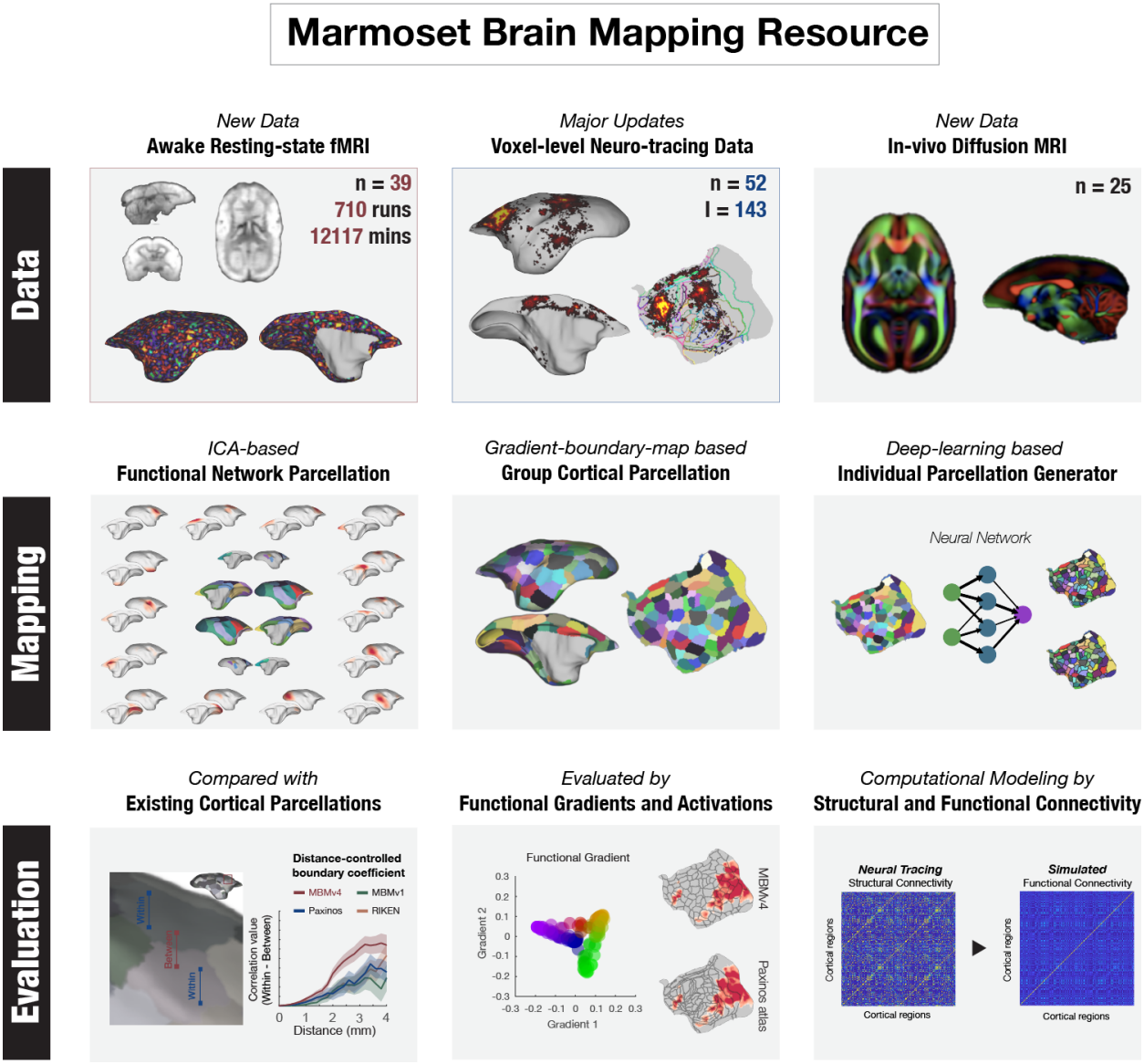

Figure 1. Outline of Marmoset Brain Mapping Resource. *This resource provides the largest available awake test-retest resting-state fMRI data, in-vivo diffusion MRI data from the same marmoset cohorts, and the most extensive neuronal tracing data mapped onto the same MRI space at the voxel/vertex level. In addition to the datasets, it also contains developed large-scale parcellation of whole-brain functional networks and population-*

based cortical parcellation (Marmoset Brain Mapping Atlas Version 4) with a deep neural network for accurate individual mapping. Finally, as the comprehensive multi-modal resource for marmoset brain research, we provide whole-brain computational modeling to investigate the relationship between structural and functional connectivity.

Mapping functional brain networks

Identifying functional networks of areas showing highly correlated fMRI signals is a key to characterizing the brain architecture. Using the independent component analysis (ICA), a data-driven approach for separating independent patterns in multivariate data, we identified 18 distinct functional networks from awake resting-state fMRI data, including 3 subcortical and 15 cortical networks (Fig. 2 and Supplementary Fig. S4). The subcortical networks included the thalamus, the striatum, and the cerebellum (Supplementary Fig. S4 P-S). All identified components showed clear neural-like patterns spatially (all peaks located in the cortical or subcortical gray matter) and temporally (no patterns of artifacts or noises), as shown in Supplementary Fig. S5.

The details of the 15 cortical networks were as follows. Six functional networks were characterized by the short-range connectivity, including the ventral somatomotor (Fig. 2A), the dorsal somatomotor (Fig. 2B), the premotor (Fig. 2C), the frontopolar (Fig. 2D), the orbitofrontal (Fig. 2E), and the parahippocampal/ temporopolar cortex (Fig. 2F). Two components are the auditory and salience-related networks, the first being primarily located in the auditory and insular cortices and weakly coupled with the anterior cingulate cortex (Fig. 2G), and the second (Fig. 2H) encompassing the anterior cingulate cortex. In addition, we also identified two trans-modal networks (Fig. 2I-J), including association areas in the dorsolateral prefrontal cortex (dlPFC), rostral premotor cortex, lateral and medial parietal cortices, and temporal cortex. According to a previous study [18], one is most likely the frontoparietal-like network (Fig. 2I), and the other is the default mode network (DMN, Fig. 2J). Importantly, the putative frontoparietal-like network has not been recognized in previous studies [19, 20]; The remaining five networks represent the first complete mapping of visual-related functional networks of the marmoset cortex (Fig. 2K-

O). Three networks included the primary visual cortex and parts of extrastriate areas related to far peripheral vision (Fig. 2K), near-peripheral vision (Fig. 2L), and the foveal vision (Fig. 2M). The other two networks involve hierarchically higher visual areas (Fig. 2N-O), such as V3, V4, the inferior temporal cortex, the adjacent polysensory temporal cortex, and visual-related frontal regions.

Based on their spatial overlap patterns and connectivity strengths (normalized Z-scores), we combined the 15 cortical networks into network-parcellation maps (Fig. 2P-Q). Due to local connectivity being stronger than long-range connectivity, the primary map (Fig. 2P-Q, top rows) is dominated by the short-range networks (*i.e.*, Fig. 2G, I, J, K, L, I, and O). Thus, we created the second one (Fig. 2P-Q, bottom rows) to cover the long-range connectivity that was not captured by the primary map. The two network-parcellation maps characterized the entire cortical networks and will likely be of great value for future functional connectivity studies of the marmoset brain.

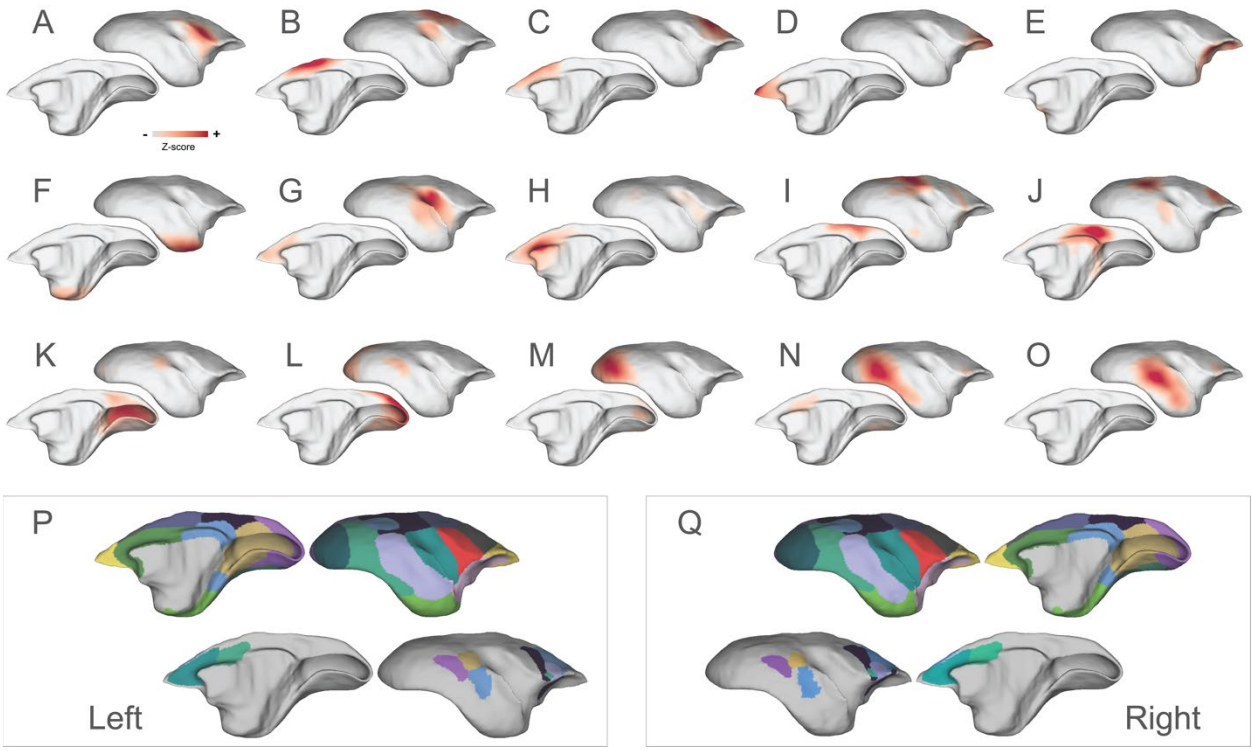

Figure 2. Identified cortical functional networks and their parcellation maps. *The networks include (A) the ventral somatomotor, (B) the dorsal somatomotor, (C) the premotor, (D) the frontal pole, (E) the orbital frontal cortex, (F) the parahippocampus and temporal pole, (G-H) the auditory and salience-related network, (I-J) two trans-modal networks, which are most likely related to the frontoparietal network and the default-mode-network, and (K-O) the visual-related networks from the primary visual cortex to functional higher-level regions. These networks were combined to form two network-parcellation maps (P-Q), which are dominated by the networks with short-range connectivity (P-Q, top rows) and with long-range connectivity (P-Q, bottom rows), respectively.*

Mapping functional connectivity boundaries

The brain network maps provided a global view of cortical functional organization. Our next aim was to characterize the cortex at a finer local scale. Here, we used the functional connectivity boundary mapping approach to identify putative borders of functional parcels [21, 22, 23], which represent an efficient way to map transitions in functional connectivity.

Population boundary maps based on the ION, the NIH, or combined datasets are visually similar, presenting clear functional connectivity borders (Fig. 3A), and were highly reproducible with average Dice's coefficients for both hemispheres: 0.7 (ION-NIH), 0.71 (ION-Both), and 0.69 (NIH-Both), respectively (see Supplementary Fig. S6). However, although consistent at the population level, boundary maps indicate variability across individuals (Fig. 3B), with an average Dice's coefficient of 0.3842 for both hemispheres (Fig. 3C-D), significantly lower than the population (the value of 0.7). We also found high across-session variability in the same individual, but more scanning runs efficiently enhanced the reproducibility (Fig. 3E). Therefore, the results suggest that both individual and across-session variability contribute to the low consistency of individual boundary maps, and the test-retest data are essential for improving the reliability of maps.

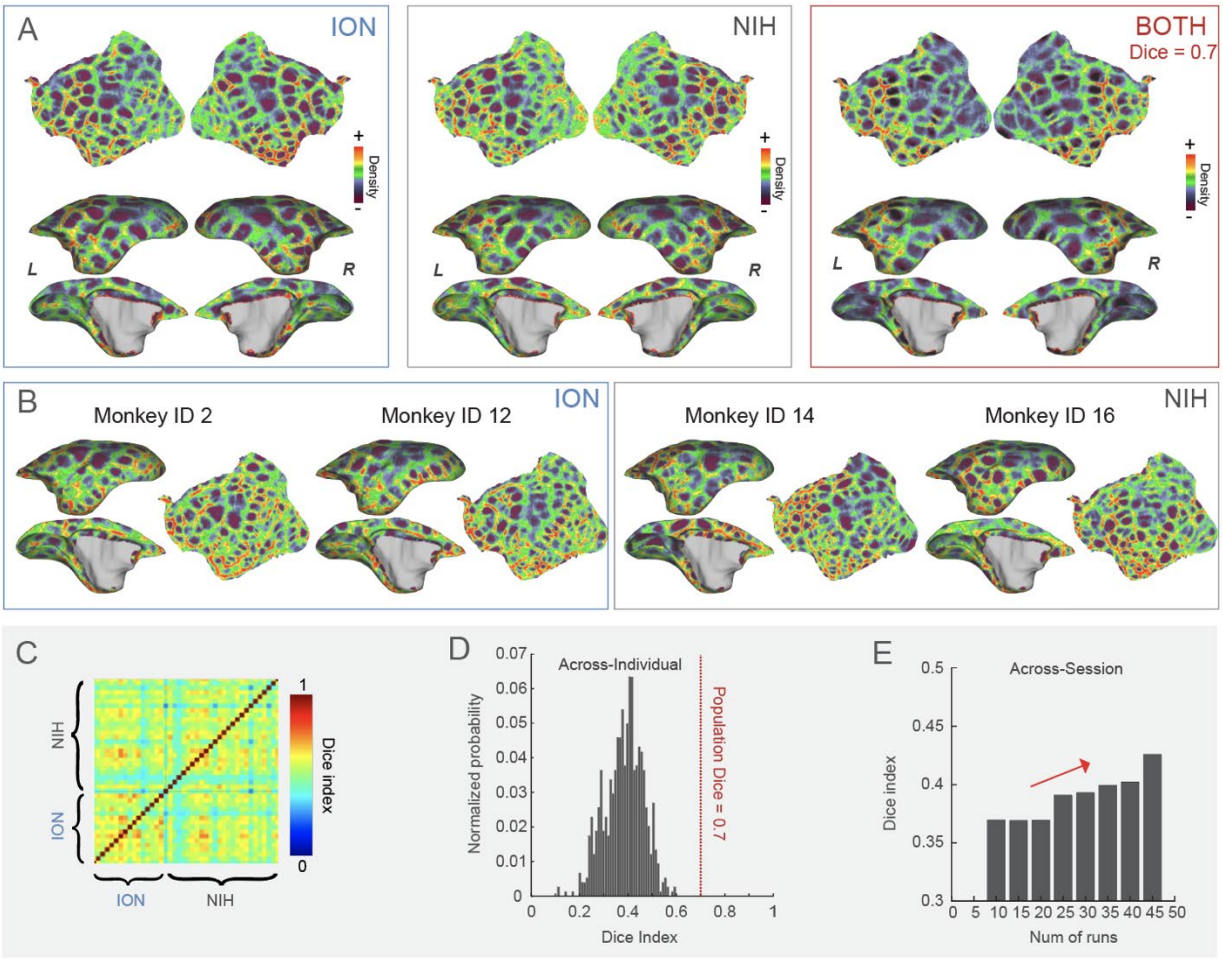

Figure 3. The functional connectivity boundary maps. *(A). The population-based boundary maps from the ION, the NIH, and the combined datasets. These maps are highly consistent, with the average Dice's coefficient of 0.7. (B). Boundary maps in the left hemisphere from four exemplar marmosets (two from the NIH cohort and two from the ION, including the flagship marmosets). (C-D). The heatmap of the average Dice's coefficients for both hemispheres between individuals and its distribution histogram. (E). The change of the average Dice's coefficients for both hemispheres with the number of runs in the same individuals.*

Generation of functional connectivity parcels (Marmoset Brain Mapping Atlas Version 4, MBMv4)

Because the population boundary maps are more reproducible than individual maps, we used the combined ION-NIH population boundary map to generate cortical functional connectivity parcels. By the detection of the local-minima [21], "watershed-flood" region growing [24], and semi-manual optimization of parcel boundaries (Fig. 4A), we obtained 96 parcels per hemisphere (Fig. 4B). Since we processed each hemisphere independently, we compared the similarity of the parcellations of the two hemispheres. The hemispherical parcellations are similar in the parcel sizes (Supplementary Fig. S7-A; Wilcoxon paired signed-rank test, N=96, p=0.7981) and functional connectivity patterns between vertices within the same parcel (Supplementary Fig. S7-B; Wilcoxon paired signed-rank test, N=96, p=0.411). This left-right symmetry corroborates the reliability of our parcel generation. For continuity with previously released resources [13, 15, 16], we named this functional connectivity-based parcellation of the cortex "*Marmoset Brain Mapping Atlas Version 4*" (MBMv4).

To estimate the validity of the generated functional parcels, we used the distance-controlled boundary coefficient (DCBC) [25]. The basic idea of DCBC is that when a boundary divides two functionally homogenous regions, for any equal distance on the cortical surface, the functional connectivity pattern between vertices within the same parcel should be higher than that between vertices in different parcels (Fig. 4C). In other words, a higher DCBC (within - between) means higher within-parcel homogeneity and higher between-parcel heterogeneity. We calculated the DCBC between the vertex pairs using a range of spatial bins (0–4 mm) with a 0.5 mm step (the spatial resolution of the rs-fMRI data). Here, we compared the fit of the functional map represented by MBMv4 with existing structural cortical parcellations, including MBMv1 atlas [15], the digital reconstruction of the Paxinos atlas [15, 26], and the RIKEN atlas [27]. The result of DCBC in Fig. 4C demonstrates that MBMv4 has the best performance for the presentation of functional connectivity (the average DCBC values were 0.0186, 0.0135, 0.0177, 0.0330

for RIKEN, MBMv1, Paxinos, and MBMv4 atlas; multiple comparisons for One-Way ANOVA $F_{(3,8556)}=22.44$, $p=1.81\times10^{-14}$).

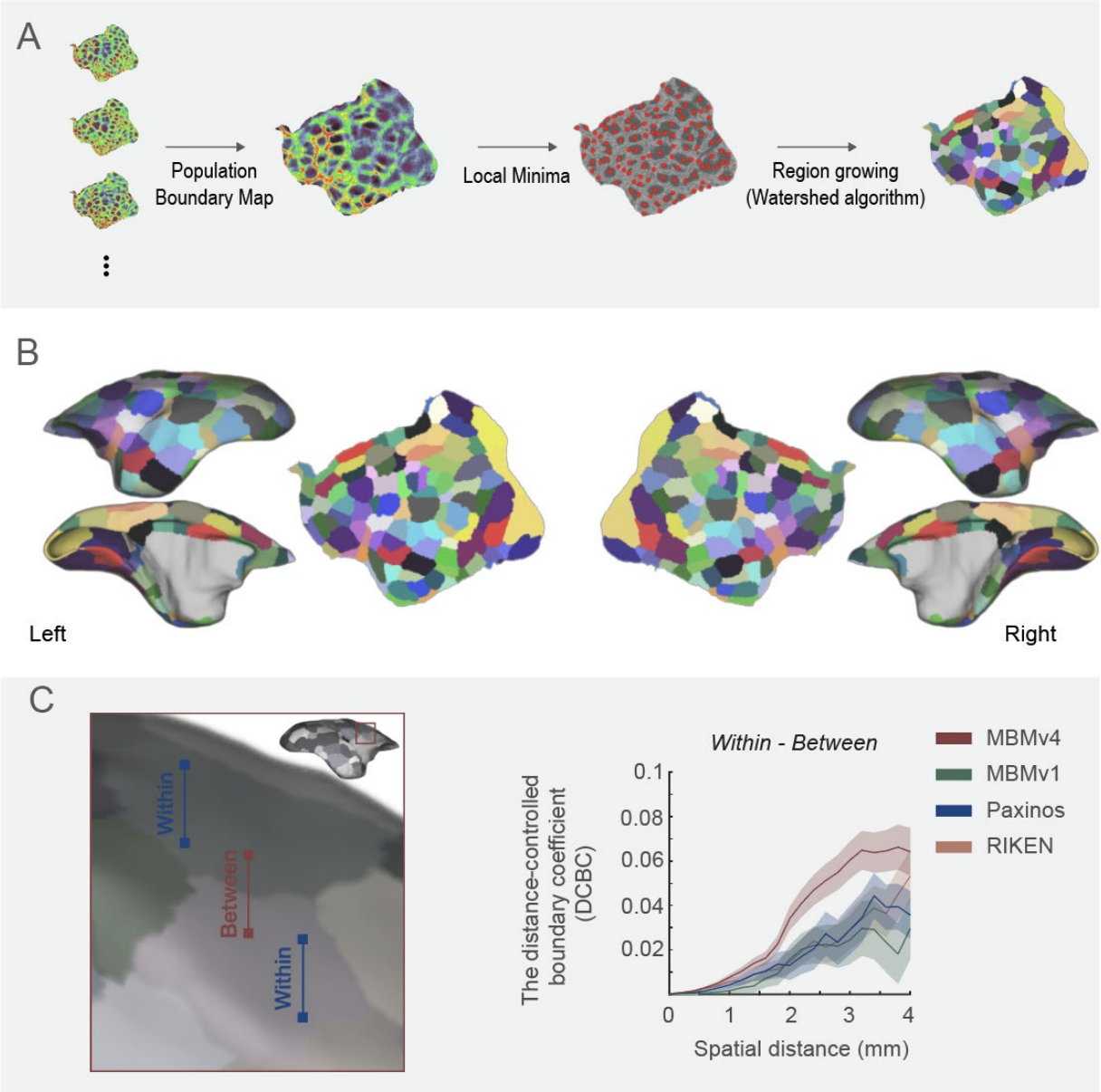

Figure 4. Marmoset Brain Mapping Atlas Version 4 (MBMv4). *(A) The processing procedure includes generating the population functional connectivity boundary maps, defining the local minima for seeding, and generating parcels by the "watershed" algorithm. (B) The resulting 96 functional connectivity parcels per hemisphere overlaid on the white matter surface and flat map of MBMv3 [16]. (C) The evaluation metric of distance-controlled boundary coefficient (DCBC). According to parcellations (Right panel: MBMv1,*

MBMv4, Paxinos, and RIKEN atlas), all pairs of voxels/vertices were categorized into "within" or "between" parcels (left panel), and the DCBC metric was calculated by the differences (within-between) in functional connectivity as the function of distance on the surface (0-4 mm in steps of 0.5 mm). Data are presented in mean +/- s.e.m.

Mapping MBMv4 in Individual Brains by Deep Neural Networks

To overcome the limitation of variable individual boundary maps (see Fig. 3C-E), we employed a deep-learning approach for the individual mapping from MBMv4 (Fig. 5A). First, based on the population-level whole-brain functional connectivity, we trained a deep neural network classifier for each parcel to learn the associated fingerprint of functional connectivity. Then, the trained networks distinguished the goal parcel for every marmoset based on the corresponding functional connectivity of the searching area, consisting of the goal parcel and its neighbors. Due to the overlap of searching areas, vertices could belong to multiple parcels. Therefore, we only kept these vertices attributed to a single parcel as the seeds for the regional growing by the "watershed" algorithm. This iterative region-growing procedure would assign all vertices to a parcel, resulting in an individual cortical parcellation.

Since individual parcellations should be reasonably close to the population definition [28, 29], we compared the population-based MBMv4 parcellation and the automatically generated individual parcellations. By calculating the percentage of vertices sharing the same labels from both hemispheres (the metric of concordance), we found that the individual parcellations from all marmosets are similar to MBMv4 with an average of 90% concordance (Fig. 5B, the violin/box plot on the left, the examples on the right). Using the test-retest dataset, we revealed the consistency of the individual parcellations across different sessions (Fig. 5C, the violin/box plot on the left, and examples on the right). The across-session analysis yielded an average of 86.7% concordance, lower than the average value of 91.3% across-individual similarities. Furthermore, we observed that the lateral prefrontal cortex and occipital-temporal cortex had higher across-individual and across-session mapping variabilities (Supplementary Fig. S8), consistent with previous

findings in human studies [21, 30]. Thus, the deep-learning approach efficiently adjusts the parcel borders to reflect the individual variabilities while maintaining high consistency with the population parcellation.

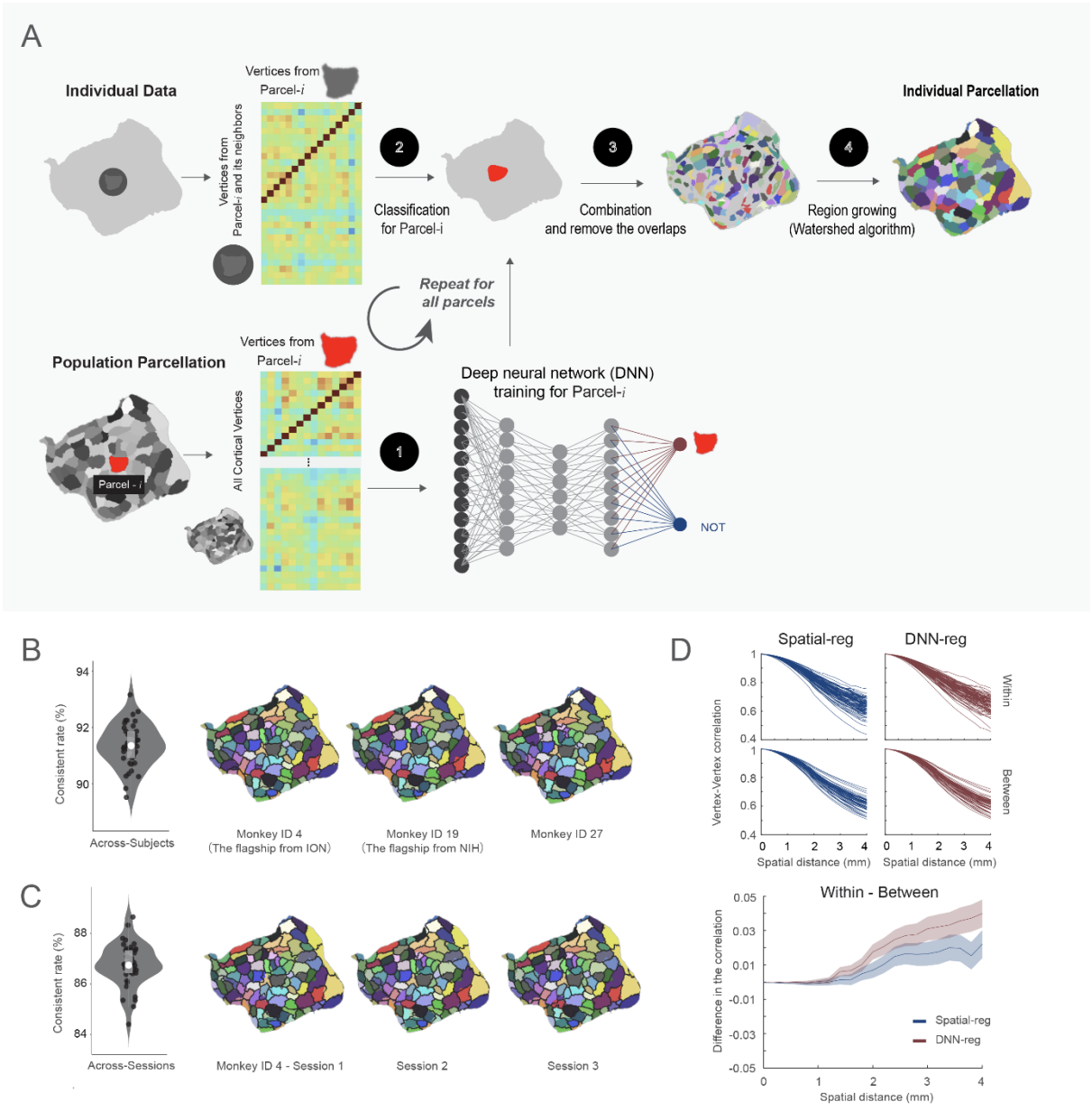

Figure 5. Mapping individual functional connectivity parcellation. *(A) An overview of individual mapping based on the deep neural network approach. (B) MBMv4 Mapping of each individual. Left panel: the concordance between the population MBMv4 and*

individual parcellations. Data are presented by the violin and the box plots (25th percentile and 75 percentile), in which the white point represents the average value; Right panel: three examples of individual parcellations. The underlay (color-coded) presents the population MBMv4, and the overlay (black border) shows the individual parcellations. (C) Mapping of MBMv4 per session. Left panel: The concordance between every individual parcellation and the corresponding parcellation using one session data; Right panel: representative parcellations of three sessions from one marmoset. The color-coded underlay represents individual parcellation, while the black border overlay shows the session-based parcellation. (D) The distance-controlled boundary coefficient (DCBC) for the individual parcellation generated by the spatial registration (Spatial-reg, blue) and the deep neural network (DNN-reg, red). Top panel: the functional connectivity for all pairs of vertices within the same parcel and between parcels for DNN-reg and Spatial-reg, respectively. Bottom panel: the comparison of DNN-reg and Spatial-reg by DCBC. Data are presented in mean +/- s.e.m.

We also used the DCBC to evaluate whether the border adjustment of the individual parcellation captured the specific features of individuals' functional connectivity patterns. We assumed that the deep learning-based method (DNN-reg) should result in a higher DCBC than the direct spatial registration of MBMv4 (Spatial-reg). Figure 5D (Top panel) presents the functional connectivity for the pairs of vertices *within* the same parcel (average correlation values within the same surface length 0-4 mm were 0.8331 and 0.8172 for DNN-reg and Spatial-reg) and *between* different parcels (average correlation values were 0.8256 and 0.8171 for DNN-reg and Spatial-reg). Thus, the DNN-reg had higher DCBC (*within-between*) than the Spatial-reg (Fig. 5D, bottom panel; the average DCBC values were 0.0167 and 0.0085 for the DNN-reg and the Spatial-reg, respectively; multiple comparisons for One-Way ANOVA $F_{(1,2512)}=20.35$, $p=6.74\times10^{-6}$). In sum, the border adjustment by the proposed deep learning network reflects individual functional connectivity patterns.

MBMv4 reflects accurate functional and topographical organizations

As evaluated from functional connectivity, MBMv4 provides a more accurate reflection of the MRI-based functional parcellation of the cortex than current histology-based atlases. To further verify this reliability, we took a task activation map during the presentation of movie [31], in which the visual field encompassed by the movie covered 10 deg × 8 deg. This activation map was then registered onto the same individual MBMv4 map and the histology-based Paxinos et al. (2012) atlas to examine the spatial overlap between the activations and functional parcels. As a result, we found that the MBMv4 has a good correspondence with task activations by visual inspection, such as the co-activation of foveal V1, MT, and temporal parcels (Fig. 6A, flat maps). Additionally, by measuring the shortest distances from every vertex in the boundary of the activation map to the atlas boundaries (MBMv4 or Paxinos boundaries), we found that the parcel borders of MBMv4 have higher consistency with the activation map than the Paxinos atlas (Fig. 6A, the scatterplots; Wilcoxon paired signed-rank test: Monkey ID 25, N=878, $p=3.07\times10^{-40}$ for the left hemisphere; N=816, $p=6.11\times10^{-26}$ for the right hemisphere. Monkey ID 15, N=826, $p=2.22\times10^{-25}$ for the left hemisphere; N=850, $p=2.95\times10^{-53}$ for the right hemisphere). Thus, MBMv4 reflects functional differences that cytoarchitectonics does not capture, possibly because the latter contains the full visual field representations. The MBMv4 provides functional localizers that can help enhance the precision of cross-species studies [32].

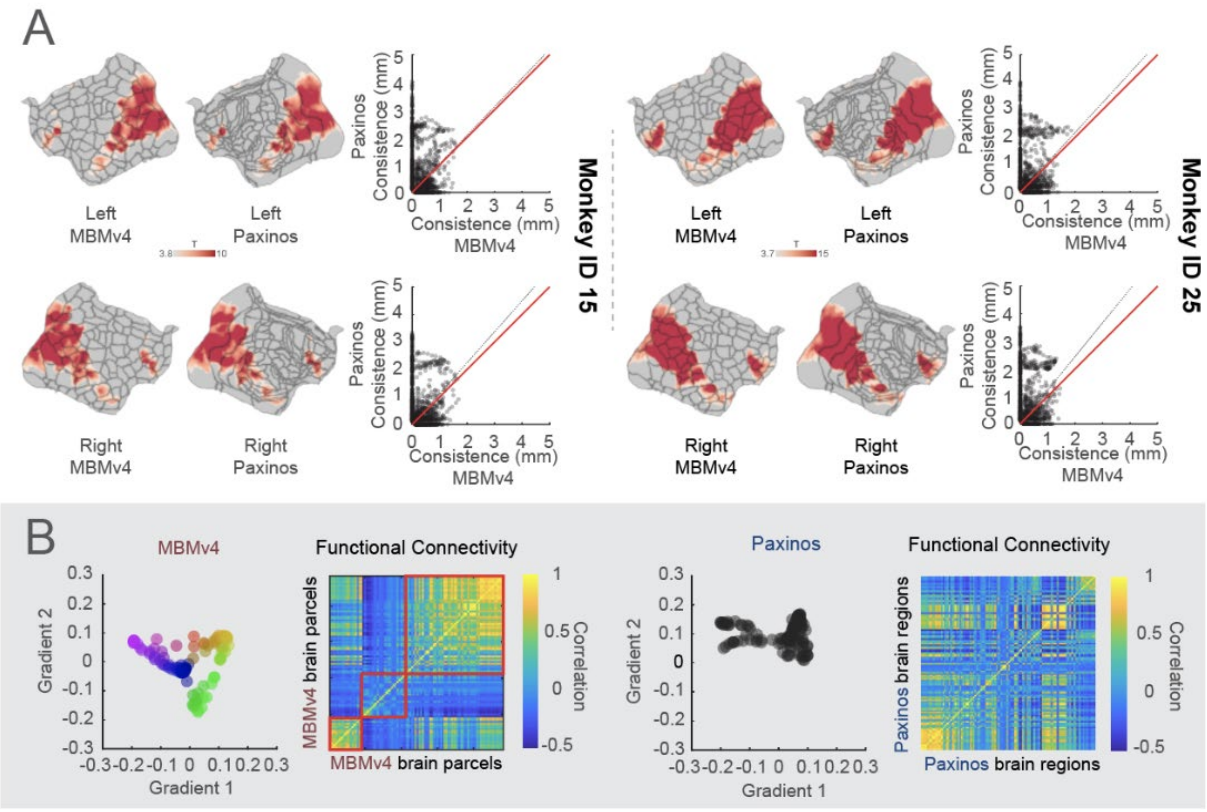

Figure 6. MBMv4 matches functional boundaries and preserves the topographical organization of the functional connectivity. *(A) The visual activation maps from two monkeys are overlaid on the parcel boundaries from individual MBMv4 parcellation and Paxinos atlas (Left panel: monkey ID 15; Right panel: monkey ID 25). The scatter plots compare the boundary matching of the MBMv4 and the Paxinos atlas with the activation maps, measured by the shortest distance from every voxel in the borders of the activation maps to the parcel borders of the MBMv4 or the Paxinos atlas. The dashed black line represents the diagonal line, and the red line represents the linear fitting line. (B) The scatter plots in the left panel are the first two axes of gradients (the color scale of dots represents the scores of the first axis for every gradient), decomposed by the functional connectivities of the MBMv4 and the Paxinos atlas (the spectrum colors denote the gradient position in this 2D space). The heatmaps of functional connectivities sorted by the scores of the first axis (gradient 1) are shown in the right panel.*

Besides the clear functional boundaries, MBMv4 also preserved the topographical organization of the functional connectivity. Recent methodological developments have allowed complex brain features to be mapped to the low-dimensional representations as gradients [33], and these gradients characterized the topographical organization of the functional brain connectome from unimodal to trans-modal networks. If the atlas complies with this topographical organization, it should be able to identify such gradients. As shown in Fig. 6B left panel, MBMv4 results in a pattern of gradient spectrum for functional connectivity. In contrast, we did not find a gradient pattern based on the Paxinos et al. (2012) atlas (right panel in Fig. 6B). Therefore, MBMv4 offers an alternative view to understanding the functional connectome of the marmoset brain by reflecting the characteristics of functional connectivity.

MBMv4 is an essential link between the functional and structural connectivity

Since MBMv4 offers a more accurate scheme to study the functional connectome, it is worth linking it to structural information to investigate relationships between structural and functional connectivity. To accomplish this, we used a whole-brain computational model [34, 35, 36]. The processing procedure is shown in Fig. 7A. We established the structural connectivity based on MBMv4 and the Paxinos et al. (2012) atlas, using either the *in-vivo* diffusion MRI or *ex-vivo* ultra-high-resolution diffusion MRI or neuronal tracing dataset. After simulating the neurodynamics of every functional parcel or brain region based on the structural connectivities, we obtained the whole-brain functional connectivity to compare with the empirical functional connectivity from the actual resting-state fMRI data. We used Pearson's correlation to measure the similarity between the simulated and the empirical functional connectivity. Additionally, we also used group-average functional connectivity as an empirical observation for the *ex-vivo* diffusion MRI and neuronal tracing dataset, and individual functional connectivity for the individual *in-vivo* diffusion MRI.

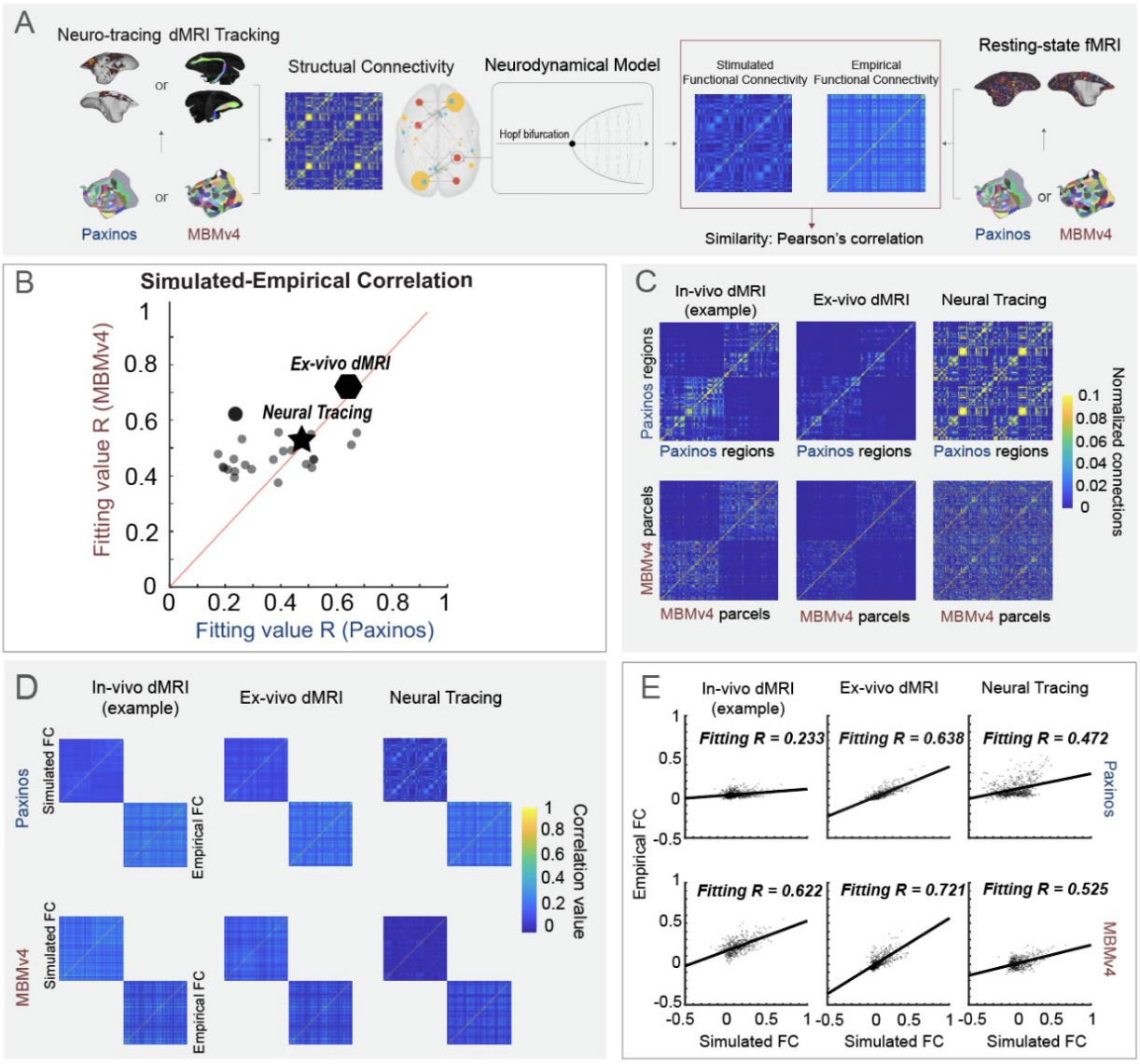

Figure 7. A computational framework links the structural-functional connectivity according to different parcellation. *(A) The application of the whole-brain modeling, including the estimation of structural connectivity from the neuronal tracing or different types of diffusion MRI (in-vivo or ex-vivo) according to the Paxinos atlas or MBMv4, the simulation of functional connectivity from structural connectivity by the Hopf bifurcation neurodynamical functions, and the similarity measure with empirical connectivity from resting-state fMRI. (B) The comparison of the fitting effect based on Paxinos atlas and MBMv4 in different spatial scales. The round dot represents an example from individual in-vivo diffusion MRI, the polygon is from ex-vivo diffusion MRI, the star is from neuronal tracing, and the solid red line represents the diagonal line. (C) The estimated structural*

connectivity labeling in (B) according to the Paxinos atlas or MBMv4. (D) The simulated functional connectivity from structural connectivity (C) and their empirical functional connectivity from actual data. (E). The correlation between the simulated and empirical functional connectivity from (D), Solid black lines represent marginal regression lines.

The modeling results suggest that accurate estimation of structural connectivity is essential for the simulation of functional connectivity. The extra high-resolution *ex-vivo* diffusion MRI with the most detailed description of structural information (the polygon in Fig. 7B and results in Fig. 7C-E) resulted in the highest similarity for MBMv4 (R=0.721) and the Paxinos atlas (R=0.638). On the other hand, due to the relatively low resolution of *in-vivo* diffusion MRI and individual differences, *in-vivo* diffusion MRI resulted in a considerable variety of simulations (all circles in Fig. 6B: the average fitting values from 25 animals were 0.4707 for MBMv4, and 0.3659 for Paxinos atlas, see an example with the best performance is in Fig. 7C-E). Based on the cellular connectivity from the aggregated neuronal tracing, we obtained a neutral performance with the correlation of 0.525 for MBMv4 and 0.472 for Paxinos atlas (the star in Fig. 7B and results in Fig. 7C-E). However, no matter which data was used for structural connectivity estimation, we always found that the modeling predicted by MBMv4 fits the empirical functional data better than the Paxinos atlas (summary in Fig. 7B; Wilcoxon paired signed-rank test: N=27, p=0.002947). Since the accuracy of the diffusion tractography may be influenced by the lengths of tracts, based on our modeling, we can reversely evaluate the structural reliability for each type of data in different connectional distances using the MBMv4. The results of modeling fitting are consistent with the prediction that the distance affects the accuracy of diffusion tractography, with low structural-functional fitting correlations for long-range connections (Supplementary Fig. S9A-C). On the contrary, the neuronal tracing data are more reliable and robust in connectivity modeling against distance (Supplementary Fig. S9D). In summary, MBMv4 preserves a crucial bridge for examining the structural and functional connectivity discrepancy.

Discussion

There are many challenges in trying to adapt well-established approaches for human neuroimaging to NHP neuroimaging [5]. The present study used effective and practical animal training and imaging protocols to scan a large cohort of marmosets. Despite the different scanners in two institutes (7T and 9.4T), the protocol produced similar data quality, suggesting the compatibility of our approach (see method for details, the Supplementary Fig. S1-S3). Given that, we pooled *in-vivo* resting-state fMRI dataset from two institutes (details in the Supplementary Table S1) to create the most comprehensive functional connectivity dataset of the NHP brain to date, which was integrated with the *in-vivo* diffusion MRI of the same cohort, as well as the highest resolution *ex-vivo* diffusion MRI [13] and the most extensive mesoscale retrograde neuronal tracing [14] available. This resource expedites the mapping of marmoset brains and will allow cross-species comparisons.

Like humans, the marmoset cerebral cortex is composed of large-scale functional networks. However, the first awake resting-state fMRI study of the marmosets [19] found only 12 functional networks (10 cortical networks), and another ICA-based study described 8 brain networks, possibly due to the influence of anesthesia [20]. Based on the most extensive awake rs-fMRI data to date, the present study mapped the large-scale functional networks and built the first network-based parcellation, providing a more comprehensive description of functional networks in the marmoset brain, including a total of 18 networks (15 cortical networks and 3 subcortical networks in Fig. 2 and the Supplementary Fig. S4-S5). Moreover, based on functional connectivity boundary maps, we also created a population-based cortical parcellation in a fine-scale (MBMv4; Fig. 4) with a total of 192 distinct parcels (96 per hemisphere). A previous study of the human cerebral cortex identified 422 discrete functional connectivity parcels using the same approach, 206 in the left hemisphere and 216 in the right hemisphere [21]. Therefore, our results align with the evidence that the number of subdivisions of the cortex increases with brain volume[37]. Thus, MBMv4 will be a helpful reference for cross-species comparison.

It is also emphasized that our functional parcels do not correspond to the traditional cytoarchitectonic definition of the cortical areas [38, 39]. Consistent with many brain parcellations by non-invasive neuroimaging [21, 28, 40, 41, 42], our defined area-level functional parcels most likely reflect a different type of computational sub-units, agreeing with the idea that the brain is organized in multiple scales [43, 44]. Therefore, compared with available structural atlases, MBMv4 captures the organization of functional connectivity accurately. For example, MBMv4 achieved better task correspondence (Fig. 6A), due to a strong link between task-fMRI and rs-fMRI [45, 46, 47]. Another evidence is the topographical gradient organization of functional connectivity (Fig. 6B). Last is better modeling simulation linking with its structural connectivity (Fig. 7).

Consistent with the previous findings in humans [21, 28, 42], the parcels defined in MBMv4 do not follow the boundaries of cytoarchitectonic areas, thus demonstrating an important difference between anatomical features and functional connectivity. For example, the somatomotor cortex is parcellated into subregions that appear to correspond to representations of the facial, forelimb, and trunk musculatures across multiple areas, and areas such as V1 and V2 are subdivided into several functional parcels according to the representation of eccentricity in visual field representation, which is contiguous across areas [48], but may include discontinuities [49]. Previous studies also revealed that some topographically organized cytoarchitectonic areas could be dissociated from the resting-state functional responses [50, 51]. Thus, the present MBMv4 should be considered a functional connectivity description, providing complementary information about the organization that cannot be observed via anatomy.

An essential goal of this study was to reflect individual characteristics by creating parcels from each individual subject's data. Although the boundary map-derived parcels could be used for individual analysis, we found that the subject boundary maps had significant variations and that the reproducibility becomes lower than the group-level map (Fig. 3). This finding emphasizes the need to acquire large amounts of data for the reliable test-retest of the individual boundary map. Given that, we developed a deep neural network

to map reliable population-level MBMv4 into every individual nonlinearly. As a result, we demonstrated good reliability in the test-retest dataset (across sessions from the same individual; see Fig. 5C) and the applications of task-fMRI activation mapping from the same individuals (Fig. 6A). Importantly, the locations of the most variable functional parcels are in the lateral prefrontal cortex and lateral temporal-occipital cortex (see Supplementary Fig. S8), corresponding to previously reported with exceptionally high inter-subject variability resting-state functional connectivities patterns [30]. Moreover, these regions co-locate with which expanded preferentially in primate evolution (Chaplin et al., 2013) and matured later in postnatal development [52]. As the resting-state functional connectivities can be altered by many biological features, including development and associated with phenotypic correlations, a better understanding of the causes of inter-subject parcel variation will be our future work.

In addition to the functional connectome mapping, we integrated all currently available structural connectome datasets, including the *in-vivo* diffusion MRI, the *ex-vivo* high-resolution diffusion MRI [13], and mesoscale tracing dataset [14]. This allowed us to investigate the relationship between functional and structural connectivity with unprecedented detail. Using whole-brain modeling [35, 36], we observed the simulated functional connectivity from the structural connectivity based on MBMv4 had a high coherence with empirical data, no matter which types of structural connectivity were used (Fig. 7B and examples Fig. 7C-E). The finding corroborates the conclusion that MBMv4 reflects meaningful computational sub-units from the view of whole-brain functional connectivity. Meanwhile, we also found room for modeling performance improvement by the detailed estimation of structural connectivity. For example, the ultra-high-resolution *ex-vivo* diffusion MRI data from a brain sample provides the most thorough structural information. Therefore, it has the best fitting results no matter which parcellation we use. Furthermore, since our modeling is simple with only two parameters that avoid overfitting simulation, the whole-brain model could be an efficient tool with broad applications to link structure and function for future studies.

Although we provided the most comprehensive multi-modal data resource for mapping the marmoset connectome, our current study still faced several limitations. First, the population used to generate the MBMv4 was sex-biased (31 males v.s. 8 females) due to the priority of colony expansion worldwide. Second, the neuronal tracing data were limited, not covering all cortical regions and missing subcortical information. Because neuronal tracing data revealed directional anatomical connections, which unidirectional diffusion tractography cannot capture, the intactness of the neuronal tracing data is critical for an accurate mapping of the future structural connectome. Third, although the resource provided the most state-of-art awake resting-state fMRI, the 0.5mm isotropic resolution may not fully capture the functional-connectivity patterns of the small marmoset brain, because of MRI technical limitations. Fourth, as robust surface reconstruction tools were not available for marmoset brains, we did not perform analysis on individual surfaces. Pooling all data onto the population-based surface may cause loss of the information about individual variability on brain morphology and reduce the accuracy of individual functional connectivity calculation and evaluation (for example, the DCBC index). Thus, automatic surface reconstruction is highly demanding for marmoset neuroimage studies. Fifth, our parcellation only used the resting-state functional connectivity information, as in many human studies[21, 28, 40]. However, more advanced approaches incorporated structural contrasts, especially the T1w/T2w myelin map and multiple task-fMRI data for multi-modal brain parcellation. Thus, combining more image modalities to improve the parcellation of the marmoset brain becomes essential in the future. Finally, although we adopted the well-established approach from human studies, our multi-modal data and analyzing atlas tools have the potential to accelerate the evolution of NHP neuroimaging research significantly.

Methods

Data Collection and Preprocessing

Animals and MRI scanning

Experimental procedures followed policies established by the Chinese Laboratory Animal – Guideline for Ethical Review of Animal Welfare (ION data) or the US Public Health Service Policy on Humane Care and Use of Laboratory Animals (NIH data). All procedures were approved by the Animal Care and Use Committee (ACUC) of the Institute of Neuroscience, Chinese Academy of Sciences (ION data) or the ACUC of the National Institute of Neurological Disorders and Stroke, National Institutes of Health (NIH data). The respective ACUC-approved protocols specify group size numbers based on a power analysis to detect differences between animals, to ensure rigor and reproducibility of the results while minimizing the number of animals used in the study. Our studies are powered to detect inter-individual differences. The experimental designs are typically 2 or 3-factor ANOVAs. Values of $p<0.05$ are considered statistically significant. The numbers of animals used is the minimum necessary to provide reliable estimates of inter-individual effects based on power considerations. Typically, sample size estimates are based on the number of animals needed to achieve a power of 0.80 for moderate effect size and 0.99 for large effect size. To ensure the psychosocial well-being of the animals, both marmoset colonies are socially housed and are offered a varied diet that includes food treats. Dedicated husbandry and veterinary teams interact with the animals daily, as part of the psychological enrichment plans approved by the ACUCs of both institutions.

The data acquisition procedure from both centers followed the same animal training protocol, 8-element radiofrequency (RF) coil design [53], and MRI scanning protocols. Thirteen marmosets (12 males and 1 female) were recruited from the ION cohort, from which we generated 62 awake resting fMRI sessions and 349 runs (17 min per run). As three of the 349 runs had extensive head motions (> 10% time points were motion censored based on the preprocessed pipeline described below), we excluded the three runs from the analysis, resulting in a total of 346 runs (see Supplementary Table S2 for the summary of the head-motion per run). Twenty-six marmosets (19 males and 7 females) were recruited from the NIH cohort to produce 51 awake resting-state fMRI sessions and 364 runs. Therefore, the NIH data and ION data had a comparable number

of valid runs. The two datasets included 39 marmosets with 113 sessions, 710 valid fMRI runs, and 12117 mins total scan time. The detailed demographic information is provided in Supplementary Table 1. All marmosets underwent a 3-to-4 week acclimatization protocol as previously described [54]. After completing the training, all marmosets were properly acclimated to laying in the sphinx position in an MRI-compatible cradle. Their heads were comfortably restrained with 3D-printed anatomically conforming helmets that allowed the resting-state fMRI (rs-fMRI) data acquisition as the animals lay relaxed in their natural resting position.

All 39 marmosets were imaged using identical rs-fMRI protocols and pulse sequences, except for a minor adjustment in the echo time (TE) made to accommodate hardware differences between the ION and the NIH gradient sets. The ION marmosets were scanned in a 9.4T/30cm horizontal MRI scanner (Bruker, Billerica, USA) equipped with a 20 cm gradient set capable of 300 mT/m gradient strength. The scanner was fitted with a 154 mm ID quadrature RF coil used for signal excitation and an 8-channel phased-array RF coil [53] custom-built for marmosets (Fine Instrument Technology, Brazil). Multiple runs of rs-fMRI data were collected in ParaVision 6.0.1 software using a 2D gradient-echo (GE) EPI sequence with the following parameters: TR = 2 s, TE = 18 ms, flip angle = 70.4°, FOV = 28 × 36 mm, matrix size = 56 × 72, 38 axial slices, slice thickness = 0.5 mm, 512 volumes (17 min) per run. The GE-EPI fMRI data were collected using two opposite phase-encoding directions (LR and RL) to compensate for EPI distortions and signal dropouts. Two sets of spin-echo EPI with opposite phase-encoding directions (LR and RL) were also collected for EPI-distortion correction (TR = 3000 ms, TE = 37.69 ms, flip angle = 90°, FOV = 28 × 36 mm, matrix size = 56 × 72, 38 axial slices, slice thickness = 0.5 mm, 8 volumes for each set). After each rs-fMRI session, a T2-weighted structural image (TR = 8000 ms, TE = 10 ms, flip angle = 90°, FOV = 28 × 36 mm, matrix size = 112 × 144, 38 axial slices, slice thickness = 0.5 mm) was scanned for co-registration purposes.

The NIH marmosets were scanned in a 7T/30cm horizontal MRI (Bruker, Billerica, USA) equipped with a 15 cm customized gradient set capable of 450 mT/m gradient strength (Resonance Research Inc., Billerica, USA). The scanner was fitted with a 110 mm ID

linear RF coil used for signal excitation and an 8-channel phased-array RF coil custom-built for marmosets [53]. During each scanning session, multiple runs of rs-fMRI data were collected in ParaVision 6.0.1. software using a 2D gradient-echo (GE) EPI sequence with the following parameters: TR = 2s, TE = 22.2 ms, flip angle = 70.4°, FOV = 28 × 36 mm, matrix size = 56 × 72, 38 axial slices, slice thickness = 0.5 mm, 512 volumes (17 min) per run. The GE-EPI fMRI data were collected using two opposite phase-encoding directions (LR and RL) to compensate for EPI distortions and signal dropouts. Two sets of spin-echo EPI with opposite phase-encoding directions (LR and RL) were also collected for EPI-distortion correction (TR = 3000 ms, TE = 36 ms, flip angle = 90°, FOV = 28 × 36 mm, matrix size = 56 × 72, 38 axial slices, slice thickness = 0.5 mm, 8 volumes for each set). After each rs-fMRI session, a T2-weighted structural image (TR = 6000 ms, TE = 9 ms, flip angle = 90°, FOV = 28 × 36 mm, matrix size = 112 × 144, 38 axis slices, slice thickness = 0.5 mm) was scanned for co-registration purposes. Furthermore, multishell diffusion MRI (DTI) datasets were collected using a 2D diffusion-weighted spin-echo EPI sequence with the following parameters: TR = 5.1 s, TE = 38 ms, number of segments = 88, FOV = 36 × 28 mm, matrix size = 72 × 56, slice thickness = 0.5 mm, a total of 400 DWI images for two-phase encodings (blip-up and blip-down) and each has 3 b values (8 b = 0, 64 b =2400, and 128 b = 4800), and the scanning duration was about 34 min. The multishell gradient sampling scheme was generated using the Q-shell sampling method [55].

Data Preprocessing

The rs-fMRI datasets were preprocessed by the customized script involving AFNI [56], FSL [57], ANTs [58], and Connectome Workbench [59]. In brief, the rs-fMRI data were slice-timing-corrected and motion-corrected by the "3dTshift" and "3dvolreg" commands of AFNI, and corrected for EPI distortions by the "top-up" command of FSL (see our examples in supplementary Fig. S10). The rs-fMRI datasets were further preprocessed by regressing linear and quadratic trends, demeaning, and censoring for motion using derivatives of motion parameters and motion-sensor regressors (any TRs and the previous TRs were censored if the detection motion was > 0.2 mm and temporal outlier > 0.1). Note that, for

the motion measurements, we calculated the weighted euclidean norm of six motion parameters with a 0.25 weight for the three rotation degrees (yaw, pitch, and roll), according to the relative head radius of the marmosets compared to humans. White matter and cerebrospinal fluid signal were removed, and the rs-fMRI datasets were band-pass filtered (0.01–0.1 Hz). The above nuisance signal regression and band-passing filtering were carried out by the "3dDeconvolve" and "3dTproject" commands in AFNI. Next, the preprocessed data were spatially normalized to the template space of our Marmoset Brain Atlas Version-3 (MBMv3) by the "*antsRegistration*" routine of ANTs [16]. The spatial normalization concatenated multiple transformations, including 1) rigid-body transformation of each fMRI run to the T2-weighted image acquired at the end of each session, 2) rigid-body transformation of T2-weighted images from each session to a cross-session averaged T2-weighted image from each animal, 3) affine and nonlinear transformation of the averaged T2-weighted image from each animal to the T2w template of our MBMv3 space. Finally, all preprocessed data were mapped to 3D brain surfaces of the MBMv3 using the Connectome Workbench (*wb_command -volume-to-surface-mapping function and ribbon constrained mapping algorithm*), normalized (subtract mean and divide by standard deviation) and concatenated per session before the boundary mapping described below. The preprocessed data were smoothed with 1mm FWHM using 3dBlurInMask (for volume data) and wb_command -cifti-smoothing (for surface data), respectively, before the network analysis and cortical parcellation.

The *in-vivo* diffusion MRI dataset was preprocessed by the DIFF_PREP, DR_BUDDI, and DR_TAMAS pipelines of TORTOISE [60]. The DIFF_PREP and DR_BUDDI routines incorporated correction for eddy-currents- and EPI-induced distortions using pairs of diffusion data acquired with opposite phase encoding (blip-up and blip-down) and the T2-weighted image and merging the preprocessed pairs into one dataset. The nonlinear spatial registration from the individual space to the DTI template of our MBMv3 space [16] was carried out using the DR_TAMAS routine of TORTOISE. The registration information was then used to transform multiple atlases to the individual space for diffusion tractography.

All diffusion trackings were performed using the iFOD2 method of the software Mrtrix3 [61]. The response function of each preprocessed diffusion MRI data was calculated by the "dhollander" method of the "dwi2response" command, and then the fibre orientation distributions (FOD) were estimated using spherical deconvolution by the multi-shell multi-tissue CSD method of the "dwi2fod" command. Finally, region-to-region tractography was performed using the iFOD2 method of the "tckgen" command. For each pair of cortical regions, diffusion tractography was conducted by using one region as the seed and the other as the target, and vice-versa. Thus, each pair of regions generated two sets of tracking probability maps, which were normalized by total streamlines selected, and the two probability maps were averaged into a single map to represent the final map of the connection of the two regions. Finally, all pairs of connections formed the whole cortical structural connectome for computational modeling.

The neuronal tracing data were mapped onto the histological NM template from our previous study [17]. The NM template is a population-based 3D cortical template generated from Nissl-stained serial sections of 20 marmosets. Since the NM template only covers the cortex and has Nissl-stain contrast and a 75μm isotropic high spatial resolution, its direct spatial transformation to our *in-vivo* MBMv3 template is inaccurate. Thus, we modified the 80μm isotropic ultra-high-resolution MTR template of our Marmoset Brain Atlas Version-2 (MBMv2) atlas [13] to remove the parts of the brain that were not covered in the NM template, including the cerebellum, brainstem, and parts of subcortical structures. This step increased the accuracy of registration between the NM template and the MBMv2 template. Then, the *ex-vivo* MTR template of the MBMv2 was transformed to the *in-vivo* myelin-map template of our MBMv3. By concatenating the two transformations (the NM-to-MBMv2 and the MBMv2-to-MBMv3), we accurately converted the neuronal tracing data from the NM template to the MRI template. We then mapped the neuronal tracing data onto the MBMv3 cortical surfaces. For the above registrations, we used the CC similarity metric as the cost functions and three-stage alignments (rigid alignment, affine alignment and non-linear SyN transformations), which were also the default options *antsRegistrationSyN.sh*. An example of registration results is shown in Supplementary Fig. S11.

Functional Networks, Cortical Parcellation and Network Modeling

Brain network identification by the Group-ICA

Independent Component Analysis (ICA) was performed by the Group-ICA routine of the GIFTI software (https://trendscenter.org/software/gift/) to identify the brain networks using a number of different component settings. First, preprocessed data without regression of nuisance covariates were group-ICA analyzed with increasing numbers of ICA components from 20 to 80 in steps of 10. We tested the reliability of different ICA methods, including the default "Infomax" ICA algorithm or "ICASSO" group-ICA method, on different datasets (the NIH dataset, the ION dataset, or combined both datasets) and obtained consistent results regardless of the ICA setting or dataset used. Finally, every resulting component from Group-ICA analyses was visually inspected and sorted according to its neuroanatomical features. Since the sorted elements were highly consistent across different settings of ICA-component numbers, we selected the best component to represent every labeled network. We identify 18 functional resting-state networks comprising of 15 cortical networks and 3 subcortical networks (Fig. 2A-O and Supplementary Fig. S4).

We combined the 15 cortical networks according to their normalized Z scores from ICA to create a cortical-network parcellation. The details include 1) the combination of networks according to their spatial locations; 2) if they have spatial overlapping, we took the highest value according to their normalized Z scores from ICA; 3) short-range (local) connectivity is usually stronger than long-range connectivity, so the single map cannot cover long-range connectivity due to the spatial overlapping. Therefore, we created a second map to cover the components with long-range connectivity that are missed in the first map. We repeat the above step but only applied to networks with long-range connections (such as Fig. 2I-K) to obtain the second map. The primary map **(**Fig. 2P-Q, top rows) is mostly contributed by the short-range networks (i.e., Fig. 1G, L, I, and O) and

the second one (Fig. 2P-Q, bottom rows) is to cover the long-range connectivity that was not captured by the primary map.

Boundary map generation

Following similar procedures to the ones described previously in a human imaging study [21], the boundary mapping of resting-state functional connectivity data was implemented in the Connectome Workbench and using customized Matlab codes (Mathworks, Natick, USA, Version 2019b; see the scripts in our open resource). First, the time course of every surface vertex for each brain hemisphere of each subject was correlated with every other surface vertex to make a correlation map. Then, a similarity map was created for every vertex by calculating pairwise spatial correlations between all correlation maps. Thirdly, the first spatial derivative was applied on the similarity map by the Connectome Workbench's function "cifti-gradient" to generate gradient maps for each brain hemisphere of each subject. Next, the gradient maps were averaged across subjects to produce the group gradient maps for each brain hemisphere. Lastly, the "watershed by flooding" algorithm was applied to identify boundaries in the gradient maps.

Test-retest evaluation of the boundary map

To compare the reliability of the boundary maps between the ION and the NIH datasets (Fig. 3A and Supplementary Fig. S6), between the individuals (Fig. 3C-E) and between runs from the same individual (Fig. 3E), we first thresholded two resulting boundary maps for each hemisphere to retain the cortical vertices most likely to be boundaries (i.e., retaining the top quartile of boundary values for a cumulative probability of 0.75) and assessed the overlap of the two thresholded boundaries by calculating the Dice's coefficient. The Dice similarity coefficient of two thresholded boundaries, A and B, is expressed as:

$$dice(A,B) = 2 * \left| \frac{intersection(A,B)}{|A| + |B|} \right|$$

The average Dice similarity coefficient is the mean of Dice similarity coefficients across hemispheres.

Cortical parcellation based on the population-level boundary map

The creation of parcels was implemented by the customized Matlab scripts (see our open resource). Firstly, based on the vertices with values smaller than their neighbors that were <5 vertices away, we identified all local minima of vertices on the boundary map as seeds for parcel creation. Then, the parcels were grown from these seeds using the "watershed algorithm" procedure as above, allowing them to expand outward from the seed until they met other parcels. Because the whole process depends on the number of seeds for parcel creation, this might result in a large number of parcels. Therefore, according to the performance, we manually defined a threshold for merging adjacent parcels, which is the 60th percentile of the values in the boundary map [21]. It means that any two adjacent parcels with an average value below this threshold were considered not sufficiently dissimilar and should be merged. Finally, according to the population-level boundary map, we visually examined remaining parcels to identify those that needed further adjustment, including eliminating vertices and spatial smoothing. The detailed manual processings for the post-optimization included 1) manually adjusting the parcel borders, 2) manually correcting wrong areal attributions of the region growing, and 3) spatial smoothing the parcel borders by 8-neighbor vertices. We finally found the resulting cortical parcellation with 96 functional parcels in each hemisphere as our Marmoset Brain Mapping Atlas Version-4 (MBMv4) in Fig. 4B.

Evaluation of cortical parcellation by the distance-controlled boundary coefficient (DCBC)

Following a previous study [25], we used the distance-controlled boundary coefficient (DCBC) as a metric to evaluate functional boundaries between our parcels. The rationale for this method is that any two points belonging to any given parcel should have more

similar functional profiles than those belonging to different parcels. Furthermore, because the functional organization varies smoothly, the correlation between two points will weaken with increasing spatial distance. Thus, we calculated the correlation coefficients for all pairs of points separated by a specific surface Euclidean distance, using 0.5 mm spatial bins (same as fMRI imaging spatial resolution) ranging from 0 to 4 mm for pairs of points residing within parcels or across different parcels (between). The DCBC defines the difference between the within-parcel and between-parcel pair correlations. A higher DCBC reflects that pairs within the same region are more functional, serving as a global parcellation measure. For the group comparison across atlases (Fig. 4C), the DCBC metrics were calculated for each participant in each spatial bin and then averaged. For the same participant comparison across atlases (Fig. 5D), the DCBC metrics were calculated for each session in each spatial bin and then averaged.

Comparison with alternative atlases

We compared our parcellation against alternative digital parcellations created by various approaches. These alternative parcellations included: (1) Paxinos atlas [62], the most commonly used atlas in marmoset brain research, which is cytoarchitectonic characterization by immunohistochemical sections, and here we used its 3D digital version [15, 26]; (2) RIKEN atlas [27]: The atlas is cytoarchitecture based on Nissl-staining contrast. (3) The first atlas version of Marmoset Brain Mapping (MBMv1) [15]: The borders were delineated based on the high-resolution diffusion MRI contrast and parcellated by a structural-connectivity-based approach.

Deep-learning-based individual parcellation generator

The group-average parcellation described in the preceding sections is desirable for generating parcellations of individual animals. Although applying our group-level parcellation to individual animals is feasible as demonstrated in the previous human study [21], we still found misalignments between individuals and cannot be highly consistent with the tendency of the group-average parcellation (MBMv4) when the scanning runs are limited (Fig. 3D-E). Therefore, inspired by previous works [28, 29], we trained a multi-layer deep learning network to classify parcels based on the fingerprints from MBMv4. There

were two assumptions for this approach: (1) We assumed that individual cortical parcels were close to the group definition after the feature-based surface registration; (2) We assumed that every identified cortical parcel should be in a single class which was the combination of the target parcel and its spatially adjacent parcels (the "searchlight" for the candidate parcel). Thus, the setup of the classifier network was straightforward. Its architecture was as follows (for the graphic reference, see Fig. 5A): for each of the 96 parcels in each hemisphere, a multi-layer deep neural network was designed, which comprised three layers (one input, five hidden, one output) and 384 hidden neurons (a reasonable compromise between accuracy and training speed for the classification). The whole-brain fingerprint of the candidate parcel from the MBMv4 worked as the training set for the network to classify whether or not each vertex in an individual ROI containing the parcel plus all of its neighbor parcels. Because of the spatial overlap of the "searchlight," we excluded the vertices belonging to multiple parcels. Then, we applied the same procedure of parcel creation as above, meaning that the borders of each identified parcel became the seeds to expand outward until they met other parcels using the "watershed by flooding" procedure. The whole process of individual parcellation was automatic and implemented using customized Matlab codes (example codes are shared via *www.marmosetbrainmapping.org/data.html*) combined with MATLAB Deep Learning Network toolbox.

Evaluation by task-activation pattern

We examined the functional relevance of the borders by evaluating the parcels contained within the fMRI activation pattern to a visual task (Fig. 6A) from our previous study [31]. A subset of animals from the NIH dataset participated in the visual-choice task, which consisted of watching 20-s-long movies (visual field is 10deg x 8deg) and 16s resting periods (206 trials for marmoset-ID15 and 280 trials for marmoset-ID25). We performed a contrast comparison between the movie-presentation blocks and the resting blocks to generate visual-task activation statistical maps for each session. A mixed-effects analysis was then applied to all statistical maps across sessions by the 3dMEMA command of AFNI to obtain a final statistical map. The map was thresholded at a voxel-wise threshold of $p < 0.05$ and a cluster-wise threshold of $p < 0.05$ for multiple comparison corrections.

To compare the similarity of the activation map and the parcellations in each hemisphere (for results, see the flat maps in Fig. 6A), we calculated the shortest Euclidean distance of every vertex/voxel in the boundary of the activation map to the vertexs/voxels in the boundary of parcels/regions from different parcellations. We considered the parcellation with the overall shortest distances of every vertex/voxel in the boundary of the activation map as the best border consistency (for results, see the scatterplots in Fig. 6A).

Evaluation by functional connectivity gradient spectrum

It is widely accepted that the cerebral cortex of multiple species, including both human and macaque primates, is organized along principal functional gradients that provide a spatial framework for the co-existence of multiple large-scale networks operating in a spectrum from unimodal to transmodal functional activity [33, 63]. Therefore, if the MBMv4 parcellation created here accurately represents the functional organization of the marmoset cortex, we can presume that it will also reveal these principal functional gradients. Thus, as in previous studies [33, 64], we followed a workflow for gradient identification: we first computed the rs-fMRI functional connectivity (RSFC) based on MBMv4. Next, the RSFC matrix $M_{x,y}$ with the same size as the atlas was made sparse (to a 10% sparsity), and a similarity matrix $A_{x,y}$ with the normalized angle was computed according to the following equation:

$$A(x,y) = 1 - \frac{\cos^{-1}\left(cossim(x,y)\right)}{\pi}$$

Next, the similarity matrix was decomposed via Laplacian transformation into a set of principal eigenvectors describing the axes of most significant variance using the following equation:

$$Lg = \lambda Dg$$

Where $D_{x,y} = \sum_y A(x,y)$, L is the graph Laplacian matrix and the eigenvectors g corresponding to the m smallest eigenvalues λ_k are used to build the new low-dimensional representation:

$$\varsigma_{LE} = [g_1, g_2, \dots, g_m]$$

Finally, the first two axes g_1, g_2 of each parcel were plotted in 2D space. Meanwhile, we used the scores g_1 to sort the functional connectivity matrix (for results, see the heatmaps in Fig. 6B).

The whole-brain modeling for the link between structural connectivity and functional connectivity

As we know, structural connectivity and functional connectivity are closely related to each other. Therefore, lack of structural evidence generally implies biological implausibility for functional connections. Testing whether the cortical parcels created above MBMv4 are accurate representations of the functional areas in the cerebral cortex requires investigation of the underlying structural connectivity. A computational model is a powerful approach to bridge structural and functional connectivity [63, 65, 66, 67, 68]. In the present study, we implemented a whole-brain model with only two free parameters from previous studies [34, 35], as outlined below (for a graphic reference, see Fig. 7A, note that the fMRI data for the modeling part is frequently unfiltered, so the model used the full band of frequency):

According to the whole cortical parcellations (192 total parcels, 96 per hemisphere from MBMv4 or 232 total regions, 116 regions per hemisphere from the Paxinos atlas), the structural connectivity between parcels/regions $C_{i,j}$ was estimated from the structural datasets (see examples in Fig. 7C), either DTI data (*in-vivo* or *ex-vivo*) or the neuronal tracing data. Then, the local dynamics for every parcel/region *j* can be properly approximated to the normal form of a Hopf bifurcation:

$$\frac{dz_j}{dt} = [a_j + iw_j]z_j + z_j|z_j|^2$$

In this equation, z_j is a complex-valued variable $z_j = x_j + y_j$, and w_j is the intrinsic signal frequency of parcel/region *j*, which ranged from 0.04-0.07Hz and was determined by the averaged peak frequency of the bandpass-filtered fMRI signals of the parcel/region *j* [35, 69, 70, 71, 72]. a_j is a bifurcation free parameter controlling the dynamics of the parcel/region j . For $a_j < 0$, the phase space presents a unique stable and is governed by noise. For $a_j > 0$, the phase space presents the stable state, giving rise to a self-sustained oscillation. For $a_j \approx 0$ the phase presents unstable state, switching back and forth and giving rise to a mixture of oscillation and noise.

The coordinated dynamics of the resting state activity for parcel/region *j* could be modeled by coupling determined by the above structural connectivity $C_{i,j}$. To ensure the oscillatory dynamics for $a_j > 0$, the structural connectivity $C_{i,j}$ should be normalized and scaled to 0.2 in a weak coupling condition before simulation starting. The coupled differential equations of the model are the following:

$$\frac{dx_j}{dt} = [a_j - x_j^2 - y_j^2]x_j - w_j y_j + G\sum_i C_{i,j}(x_i - x_j)\beta\eta_j(t)$$

$$\frac{dy_j}{dt} = [a_j - x_j^2 - y_j^2]y_j + w_j x_j + G\sum_i C_{i,j}(y_i - y_j)\beta\eta_j(t)$$

In this equation, G is another free parameter representing the fixed global coupling factor that scales structural connectivity $C_{i,j}$. η_j represents additive Gaussian noise in each parcel/region and is scaled by a factor β fixed at 0.04 according to previous studies [35]. Euler-Maruyama algorithm integrated these equations with a time step of 0.1 seconds to accelerate simulation [73].

The free bifurcation parameter a_j for parcel/region *j* could be locally optimized based on fitting the spectral information of the empirical BOLD signals. To achieve this, we filtered the empirical BOLD data in the 0.04–0.25Hz band and calculated the power spectrum $p_j(f)$ for each parcel *j* as below:

$$p_j = \frac{\int_{0.04}^{0.07} p_j(f)df}{\int_{0.04}^{0.25} p_j(f)df}$$

and updated the local bifurcation parameter a_j by a gradient descendent strategy:

$$a_j = a_j + \eta\left(p_j^{empirical} - p_j^{simulated}\right)$$

We applied the above optimization process to receive the best bifurcation parameters a_j of every parcel/region defined in the parcellations. Once we found the optimized set of bifurcation parameters a_j, we adjusted the free parameter *G* within the range of 0-8 in steps of 0.1 according to a reasonable compromise from previous studies [35, 73] to simulate the same number of sessions for each animal and the same number of animals. To compare the performance in different atlases, we just needed to compare fitting (similarity) metrics, Pearson's correlation coefficient between the simulated functional connectivity and the one used for the empirical data, when we fixed the same value of parameter *G*.

Since the distributions of the optimal bifurcation parameter a are identical in different parcellations MBMv4 or Paxinos atlas (see Supplementary Fig. S12, one way ANOVA $F_{(1,11986)}$=9.09, p=0.26), we selected the best free parameter *G* from the Paxinos atlas for comparison performance with our MBMv4 (see results in Fig. 7B, examples in Fig. 7D-E). Moreover, we also selected the group-averaged functional connectivity from all individuals as the empirical observable for the ultra-high resolution diffusion MRI and neuronal tracing datasets and the individual functional connectivity for the corresponding *in-vivo* diffusion MRI.

Data availability

All NIH and ION resting-state fMRI, diffusion MRI, and neuronal tracing datasets are available at *www.marmosetbrainmapping.org/data.html*. The volume data are in NIFTI format, and the surface data are in CIFTI format. The raw MRI data are provided in the standard BIDS format for cross-platform sharing. In addition, data with different preprocessing, including a minimal preprocessing pipeline, are provided for analyzing purposes.

Code availability

The codes and analyzing pipelines (with code examples) used in this study are available at *www.marmosetbrainmapping.org/data.html*.

Acknowledgments

We thank Kaiwei Zhang and Binshi Bo at 9.4T core facility (CEBSIT) for assistance in data collection of the ION data, Lisa Zhang for the assistance in data collection of the NIH 7T data, Xiaojia Zhu for the assistance in organizing MRI data format, and the NIH Fellows Editorial Board for the editorial assistance. In addition, the following funding sources supported the study:

The study was supported by the grants from the National Key Research and Development Program (2021ZD0203903), the National Natural Science Foundation of China (No. 32171088 to CL, 81771821 to ZL), the Pennsylvania Department of Health Commonwealth Universal Research Enhancement (CURE.) Tobacco Settlement Appropriation – Phase 18 (Grant SAP4100083102 to AS), the Australian Research Council (DP110101200, DP140101968, CE140100007 to MR), the National Science Centre (2019/35/D/NZ4/03031 to PM), NIH Intramural Research Programs (ZIA

NS003041 to AS and CY, ZICMH002888 to DG), CAS Pioneer Hundred Talents Program, Strategic Priority Research Program of the Chinese Academy of Sciences (No. XDB32030100 to ZL), the Shanghai Municipal Science and Technology Major Project (No. 2018SHZDZX05 to CL and ZL), International Neuroinformatics Coordinating Facility Seed Funding Grant (to PM and MR), a Spanish research project funded by the Spanish Ministry of Science, Innovation, and Universities (MCIU), State Research Agency (AEI), and European Regional Development Funds (FEDER) (ref. PID2019-105772GB-I00 AEI FEDER EU to GD), HBP SGA3 Human Brain Project Specific Grant Agreement 3 (grant agreement no. 945539 to GD), and the EU H2020 FET Flagship program and SGR Research Support Group support (ref. 2017 SGR 1545 to GD).

Author contributions

CL, XT, ZL, AS, and MR designed and supervised the study; YC and ZL collected the ION MRI data; DS, CL, CC and XT collected the NIH MRI data; MR and PM collected the neuronal tracing data; CL, XT, CT, ZL, and KS preprocessed and organized the MRI data; PM, CL, XT, and HJ preprocessed the neuronal tracing data; CL and XT constructed the functional-network maps; CL, XT and MR constructed and evaluated the cortical parcellation maps; XT, CL, YP, and GD conducted the computational modeling; DG and CL implemented the atlas and resources into AFNI/SUMA. XT and CL wrote the original draft, and CL, XT, AS, MR, PM, ZL, GD, CC, and DG revised the draft.

References

1. Buffalo EA, Movshon JA, Wurtz RH. From basic brain research to treating human brain disorders. *Proc Natl Acad Sci U S A*, (2019).

2. Thiebaut de Schotten M, Croxson PL, Mars RB. Large-scale comparative neuroimaging: Where are we and what do we need? *Cortex* **118**, 188-202 (2019).

3. Buckner RL, Margulies DS. Macroscale cortical organization and a default-like apex transmodal network in the marmoset monkey. *Nat Commun* **10**, 1976 (2019).

4. Smith SM*, et al.* Resting-state fMRI in the Human Connectome Project. *Neuroimage* **80**, 144-168 (2013).

5. Milham MP*, et al.* An Open Resource for Non-human Primate Imaging. *Neuron* **100**, 61-74 e62 (2018).

6. Hudetz AG. General anesthesia and human brain connectivity. *Brain Connect* **2**, 291-302 (2012).

7. Milham M*, et al.* Accelerating the Evolution of Nonhuman Primate Neuroimaging. *Neuron* **105**, 600-603 (2020).

8. Milham M*, et al.* Toward next-generation primate neuroscience: A collaboration-based strategic plan for integrative neuroimaging. *Neuron*, (2021).

9. Messinger A*, et al.* A collaborative resource platform for non-human primate neuroimaging. *Neuroimage* **226**, 117519 (2021).

10. Okano H. Current Status of and Perspectives on the Application of Marmosets in Neurobiology. *Annu Rev Neurosci* **44**, 27-48 (2021).

11. Walker J, MacLean J, Hatsopoulos NG. The marmoset as a model system for studying voluntary motor control. *Dev Neurobiol* **77**, 273-285 (2017).

12. Matsuzaki M, Ebina T. Common marmoset as a model primate for study of the motor control system. *Curr Opin Neurobiol* **64**, 103-110 (2020).

13. Liu C*, et al.* A resource for the detailed 3D mapping of white matter pathways in the marmoset brain. *Nat Neurosci* **23**, 271-280 (2020).

14. Majka P*, et al.* Open access resource for cellular-resolution analyses of corticocortical connectivity in the marmoset monkey. *Nat Commun* **11**, 1133 (2020).

15. Liu C*, et al.* A digital 3D atlas of the marmoset brain based on multi-modal MRI. *Neuroimage* **169**, 106-116 (2018).

16. Liu C, Yen CC, Szczupak D, Tian X, Glen D, Silva AC. Marmoset Brain Mapping V3: Population multi-modal standard volumetric and surface-based templates. *Neuroimage* **226**, 117620 (2021).

17. Majka P*, et al.* Histology-Based Average Template of the Marmoset Cortex With Probabilistic Localization of Cytoarchitectural Areas. *Neuroimage* **226**, 117625 (2021).

18. Liu C, Yen CC, Szczupak D, Ye FQ, Leopold DA, Silva AC. Anatomical and functional investigation of the marmoset default mode network. *Nat Commun* **10**, 1975 (2019).

19. Belcher AM*, et al.* Large-scale brain networks in the awake, truly resting marmoset monkey. *J Neurosci* **33**, 16796-16804 (2013).

20. Ghahremani M, Hutchison RM, Menon RS, Everling S. Frontoparietal Functional Connectivity in the Common Marmoset. *Cereb Cortex* **27**, 3890-3905 (2017).

21. Gordon EM, Laumann TO, Adeyemo B, Huckins JF, Kelley WM, Petersen SE. Generation and Evaluation of a Cortical Area Parcellation from Resting-State Correlations. *Cereb Cortex* **26**, 288-303 (2016).

22. Cohen AL*, et al.* Defining functional areas in individual human brains using resting functional connectivity MRI. *Neuroimage* **41**, 45-57 (2008).

23. Wig GS, Laumann TO, Petersen SE. An approach for parcellating human cortical areas using resting-state correlations. *Neuroimage* **93 Pt 2**, 276-291 (2014).

24. Cousty J, Bertrand G, Najman L, Couprie M. Watershed Cuts: Minimum Spanning Forests and the Drop of Water Principle. *Ieee T Pattern Anal* **31**, 1362-1374 (2009).

25. King M, Hernandez-Castillo CR, Poldrack RA, Ivry RB, Diedrichsen J. Functional boundaries in the human cerebellum revealed by a multi-domain task battery. *Nat Neurosci* **22**, 1371-1378 (2019).

26. Majka P*, et al.* Towards a comprehensive atlas of cortical connections in a primate brain: Mapping tracer injection studies of the common marmoset into a reference digital template. *J Comp Neurol* **524**, 2161-2181 (2016).

27. Woodward A*, et al.* The Brain/MINDS 3D digital marmoset brain atlas. *Sci Data* **5**, 180009 (2018).

28. Glasser MF*, et al.* A multi-modal parcellation of human cerebral cortex. *Nature* **536**, 171-178 (2016).

29. Hacker CD*, et al.* Resting state network estimation in individual subjects. *Neuroimage* **82**, 616-633 (2013).

30. Mueller S*, et al.* Individual variability in functional connectivity architecture of the human brain. *Neuron* **77**, 586-595 (2013).

31. Tian X, Silva AC, Liu C. The Brain Circuits and Dynamics of Curiosity-Driven Behavior in Naturally Curious Marmosets. *Cereb Cortex* **31**, 4220-4232 (2021).

32. Russ BE*, et al.* Common functional localizers to enhance NHP & cross-species neuroscience imaging research. *Neuroimage* **237**, 118203 (2021).

33. Margulies DS*, et al.* Situating the default-mode network along a principal gradient of macroscale cortical organization. *Proc Natl Acad Sci U S A* **113**, 12574-12579 (2016).

34. Ipina IP*, et al.* Modeling regional changes in dynamic stability during sleep and wakefulness. *Neuroimage* **215**, 116833 (2020).

35. Deco G, Kringelbach ML, Jirsa VK, Ritter P. The dynamics of resting fluctuations in the brain: metastability and its dynamical cortical core. *Sci Rep* **7**, 3095 (2017).

36. Deco G, Jirsa V, McIntosh AR, Sporns O, Kotter R. Key role of coupling, delay, and noise in resting brain fluctuations. *Proc Natl Acad Sci U S A* **106**, 10302-10307 (2009).

37. Changizi MA, Shimojo S. Parcellation and area-area connectivity as a function of neocortex size. *Brain Behav Evol* **66**, 88-98 (2005).

38. Kaas JH. The organization of neocortex in mammals: implications for theories of brain function. *Annu Rev Psychol* **38**, 129-151 (1987).

39. Amunts K, Zilles K. Architectonic Mapping of the Human Brain beyond Brodmann. *Neuron* **88**, 1086-1107 (2015).

40. Schaefer A*, et al.* Local-Global Parcellation of the Human Cerebral Cortex from Intrinsic Functional Connectivity MRI. *Cereb Cortex* **28**, 3095-3114 (2018).

41. Van Essen DC, Glasser MF, Dierker DL, Harwell J, Coalson T. Parcellations and hemispheric asymmetries of human cerebral cortex analyzed on surface-based atlases. *Cereb Cortex* **22**, 2241-2262 (2012).

42. Van Essen DC, Glasser MF. Parcellating Cerebral Cortex: How Invasive Animal Studies Inform Noninvasive Mapmaking in Humans. *Neuron* **99**, 640-663 (2018).

43. van den Heuvel MP, Yeo BTT. A Spotlight on Bridging Microscale and Macroscale Human Brain Architecture. *Neuron* **93**, 1248-1251 (2017).

44. Churchland PS, Sejnowski TJ. Perspectives on cognitive neuroscience. *Science* **242**, 741-745 (1988).

45. Smith SM*, et al.* Correspondence of the brain's functional architecture during activation and rest. *Proc Natl Acad Sci U S A* **106**, 13040-13045 (2009).

46. Mennes M*, et al.* Inter-individual differences in resting-state functional connectivity predict task-induced BOLD activity. *Neuroimage* **50**, 1690-1701 (2010).

47. Tavor I, Parker Jones O, Mars RB, Smith SM, Behrens TE, Jbabdi S. Task-free MRI predicts individual differences in brain activity during task performance. *Science* **352**, 216-220 (2016).

48. Rosa MG, Tweedale R. Brain maps, great and small: lessons from comparative studies of primate visual cortical organization. *Philos Trans R Soc Lond B Biol Sci* **360**, 665-691 (2005).

49. Yu HH, Rowley DP, Price NSC, Rosa MGP, Zavitz E. A twisted visual field map in the primate dorsomedial cortex predicted by topographic continuity. *Sci Adv* **6**, (2020).

50. Long X, Goltz D, Margulies DS, Nierhaus T, Villringer A. Functional connectivity-based parcellation of the human sensorimotor cortex. *Eur J Neurosci* **39**, 1332-1342 (2014).

51. Rao SM*, et al.* Somatotopic mapping of the human primary motor cortex with functional magnetic resonance imaging. *Neurology* **45**, 919-924 (1995).

52. Sawiak SJ*, et al.* Trajectories and Milestones of Cortical and Subcortical Development of the Marmoset Brain From Infancy to Adulthood. *Cereb Cortex* **28**, 4440-4453 (2018).

53. Papoti D, Yen CC, Hung CC, Ciuchta J, Leopold DA, Silva AC. Design and implementation of embedded 8-channel receive-only arrays for whole-brain MRI and fMRI of conscious awake marmosets. *Magn Reson Med* **78**, 387-398 (2017).

54. Silva AC*, et al.* Longitudinal functional magnetic resonance imaging in animal models. *Methods Mol Biol* **711**, 281-302 (2011).

55. Caruyer E, Lenglet C, Sapiro G, Deriche R. Design of multishell sampling schemes with uniform coverage in diffusion MRI. *Magn Reson Med* **69**, 1534-1540 (2013).

56. Cox RW. AFNI: what a long strange trip it's been. *Neuroimage* **62**, 743-747 (2012).

57. Jenkinson M, Beckmann CF, Behrens TE, Woolrich MW, Smith SM. Fsl. *Neuroimage* **62**, 782-790 (2012).

58. Tustison N*, et al.* Multivariate Analysis of Diffusion Tensor Imaging and Cortical Thickness Maps in a Traumatic Brain Injury (Tbi) Cohort Using Advanced Normalization Tools (Ants). *J Neurotraum* **28**, A111-A111 (2011).

59. Marcus DS*, et al.* Informatics and data mining tools and strategies for the human connectome project. *Front Neuroinform* **5**, 4 (2011).

60. Pierpaoli C. Quantitative brain MRI. *Top Magn Reson Imaging* **21**, 63 (2010).

61. Tournier J-D, Calamante F, Connelly A. MRtrix: Diffusion tractography in crossing fiber regions. *International Journal of Imaging Systems and Technology* **22**, 53-66 (2012).

62. Paxinos G, Watson C, Petrides M, Rosa M, Tokuno H. *The marmoset brain in stereotaxic coordinates*. Elsevier Academic Press (2012).

63. Wang P*, et al.* Inversion of a large-scale circuit model reveals a cortical hierarchy in the dynamic resting human brain. *Sci Adv* **5**, eaat7854 (2019).

64. Vos de Wael R*, et al.* BrainSpace: a toolbox for the analysis of macroscale gradients in neuroimaging and connectomics datasets. *Commun Biol* **3**, 103 (2020).

65. Hansen EC, Battaglia D, Spiegler A, Deco G, Jirsa VK. Functional connectivity dynamics: modeling the switching behavior of the resting state. *Neuroimage* **105**, 525-535 (2015).

66. Breakspear M. Dynamic models of large-scale brain activity. *Nat Neurosci* **20**, 340-352 (2017).

67. Schirner M, McIntosh AR, Jirsa V, Deco G, Ritter P. Inferring multi-scale neural mechanisms with brain network modelling. *Elife* **7**, (2018).

68. Honey CJ*, et al.* Predicting human resting-state functional connectivity from structural connectivity. *Proc Natl Acad Sci U S A* **106**, 2035-2040 (2009).

69. Ponce-Alvarez A, Deco G, Hagmann P, Romani GL, Mantini D, Corbetta M. Resting-state temporal synchronization networks emerge from connectivity topology and heterogeneity. *PLoS Comput Biol* **11**, e1004100 (2015).

70. Achard S, Salvador R, Whitcher B, Suckling J, Bullmore E. A resilient, low-frequency, small-world human brain functional network with highly connected association cortical hubs. *J Neurosci* **26**, 63-72 (2006).

71. Buckner RL*, et al.* Cortical hubs revealed by intrinsic functional connectivity: mapping, assessment of stability, and relation to Alzheimer's disease. *J Neurosci* **29**, 1860-1873 (2009).

72. Glerean E, Salmi J, Lahnakoski JM, Jaaskelainen IP, Sams M. Functional magnetic resonance imaging phase synchronization as a measure of dynamic functional connectivity. *Brain Connect* **2**, 91-101 (2012).

73. Sanz Perl Y*, et al.* Perturbations in dynamical models of whole-brain activity dissociate between the level and stability of consciousness. *PLoS Comput Biol* **17**, e1009139 (2021).

Supplementary Information

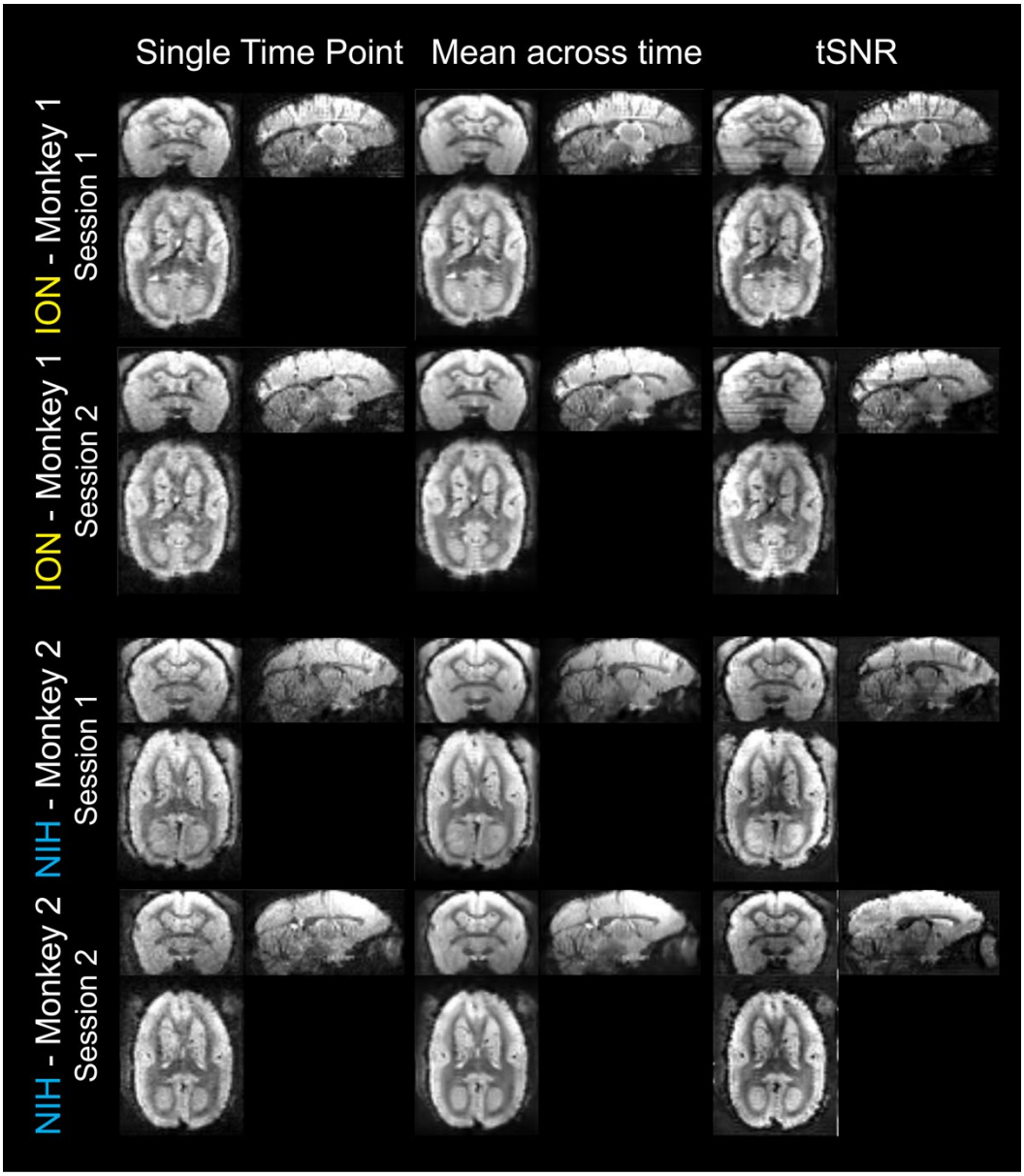

Figure S1. Example images of the ION and the NIH datasets. Single time points, mean images (averaged across time for one fMRI run), and tSNR images (calculated from one fMRI run) are presented for four sessions of two flagship monkeys from ION and NIH, respectively. The tSNR image of each session was calculated by 3dTstat of AFNI.

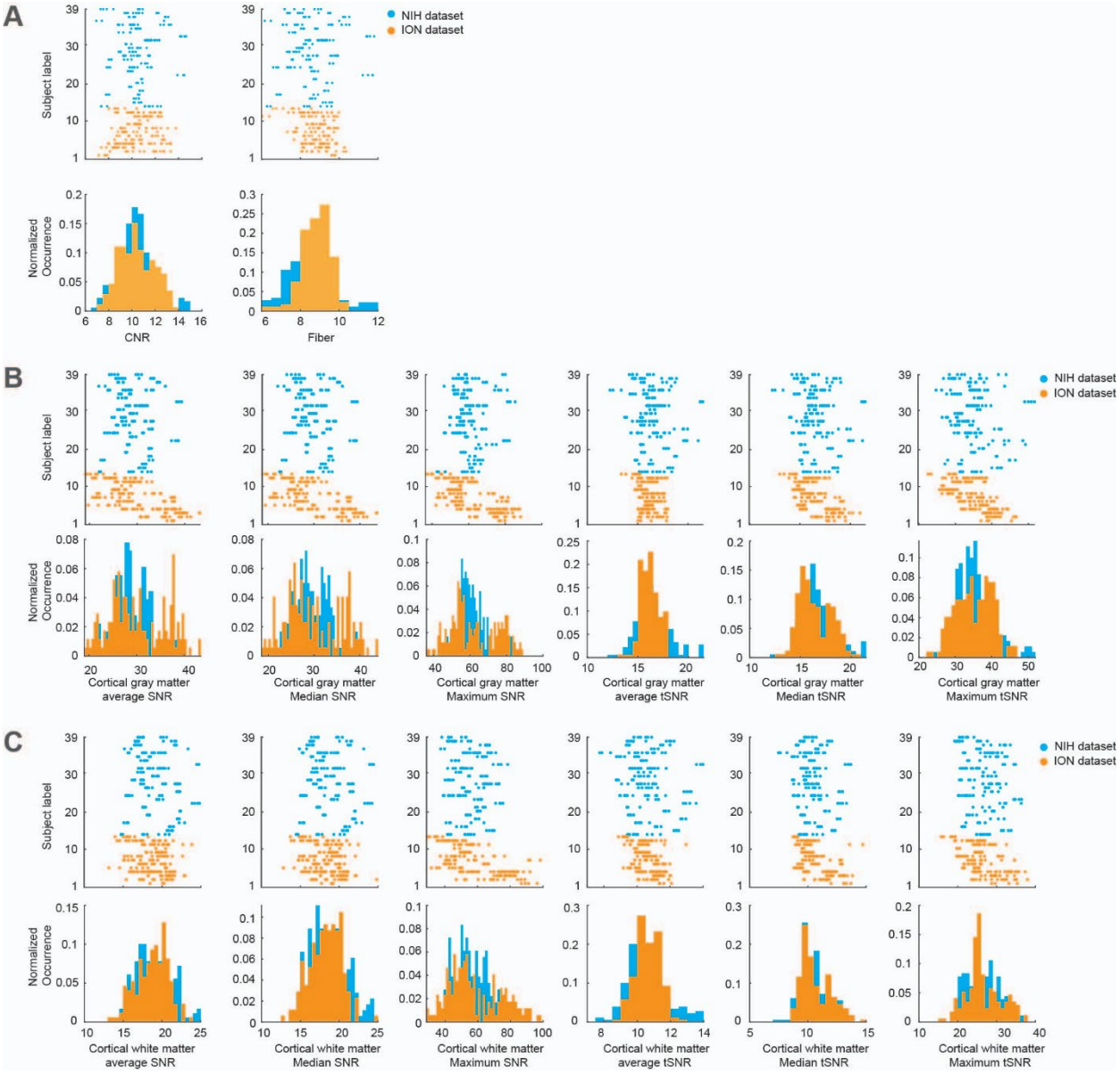

Figure S2. Similar quality measurements of the ION and the NIH datasets. (A) the raster plots and their histograms present the CNR (Contrast to Noise Ratio: the mean of the gray matter intensity values minus the mean of the white matter intensity values divided by the standard deviation of the values outside the brain) and the Fiber (Foreground to Background Energy Ratio: the variance of voxels inside the brain divided by the variance of voxels outside the brain) of two datasets (the blue represents the results from the NIH dataset, and the yellow represents the results from the ION dataset); the results of the Wilcoxon rank test between two datasets (N-NIH =180 N-ION =172) are p=0.45 and p=0.11, respectively. (B) the raster plots and their histograms present the average SNR, median SNR and max SNR, average tSNR, median tSNR and max tSNR of the cortical gray matter from two datasets (N-NIH =180 N-ION =172). The Wilcoxon rank tests for SNR are p=0.259 p=0.824 and p=0.968; and for tSNR are p=0.435 p=0.625 and p=0.2, respectively. (C) presents the average SNR, median SNR and max SNR,

average tSNR, median tSNR and max tSNR of cortical white matter from two datasets (N-NIH =180 N-ION =172). The Wilcoxon rank tests for SNR are p=0.712 p=0.32 and p=0.42; and for tSNR are p=0.062 p=0.086 and p=0.908, respectively. The NIH and the ION datasets have no significant difference in the above QA measurements. The tSNR image of each session was calculated by 3dTstat of AFNI. The SNR and tSNR values were calculated by “the mean value of gray matter voxels divided by the standard deviation of background noises”.

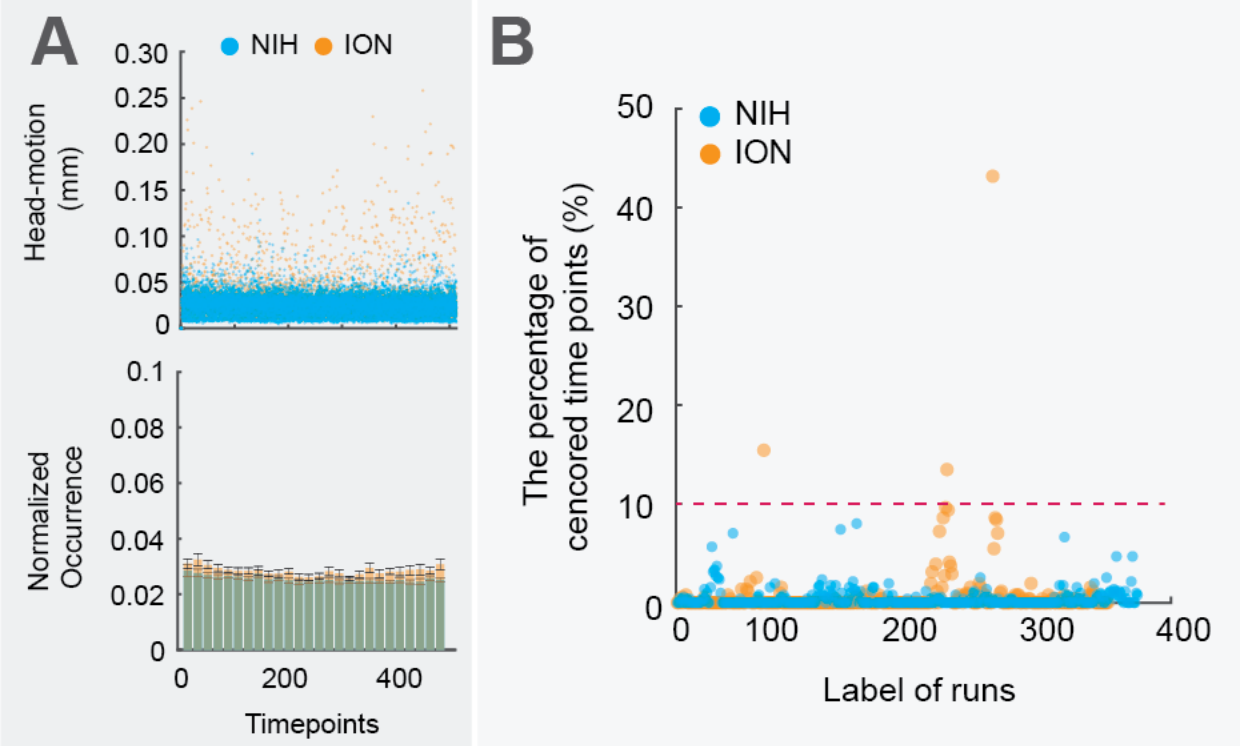

Figure S3. Head motions of the ION and the NIH datasets. (A) the top panel presents head-motion (weighted euclidean norm of six motion parameters) across timepoints of different datasets (the blue represents the NIH dataset, and the yellow is the ION dataset). Each dot is the head-motion measure of each fMRI at a one-time point. The bottom panel presents the histogram statistics from each dataset (error bar represents 95% confidence interval), which indicates head-motion levels are similar across datasets. (B) presents the percentage of censored time points (motion > 0.2mm and temporal outlier > 0.1) for each fMRI. Most animals and fMRI runs (710 runs) have low head-motion and censored time points, suggesting the effectiveness of our head-constrained and training approaches. Note that the three fMRI runs with extensive head motions (more than 10% time points were censored) were excluded from our analysis and from the total number of valid runs (710) reported in our manuscript, although we included the three runs in the release of source (raw) data.

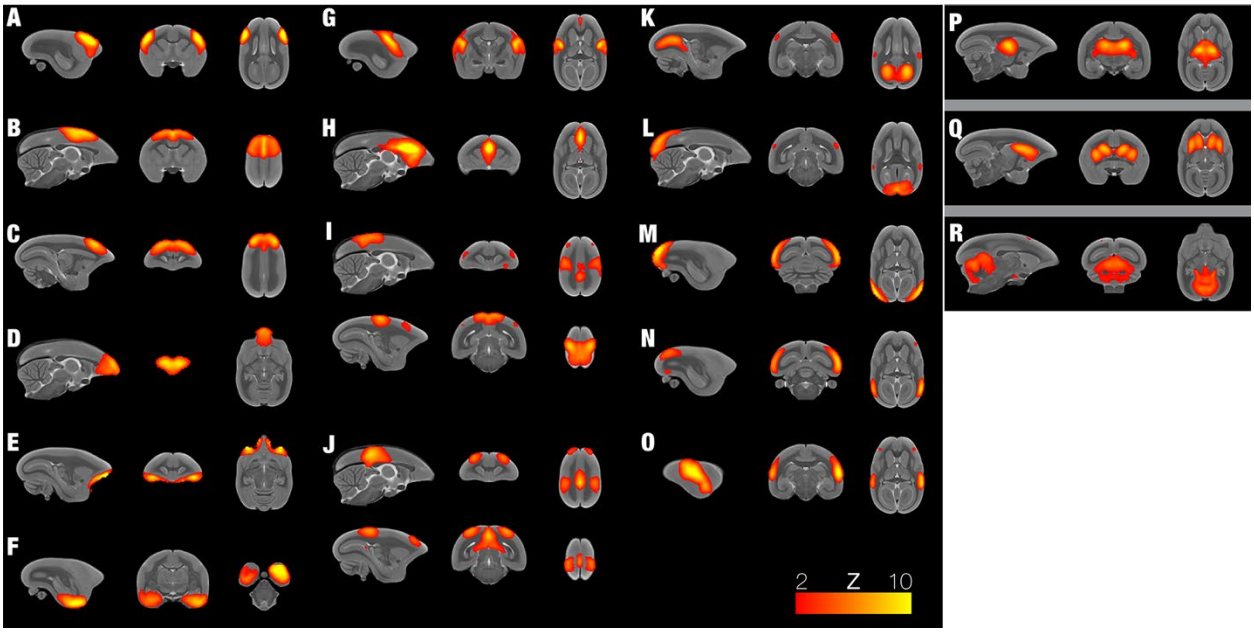

Figure S4. Identified resting-state functional networks. We found 19 networks by group-ICA analysis, including (A) the ventral somatomotor, (B) the dorsal somatomotor, (C) the premotor, (D) the frontal pole, (E) the orbital frontal cortex, (F) the parahippocampus/temporal pole, (G-H) the salience-related network, (I-J) two trans-modal networks, which are frontoparietal (I) and the default-mode-network-related (J), the visual-related networks from primary visual cortex (K-M) to functional higher-level regions (N-O) and subcortical networks, the thalamus (P), the striatum (Q), and the cerebellum (R).

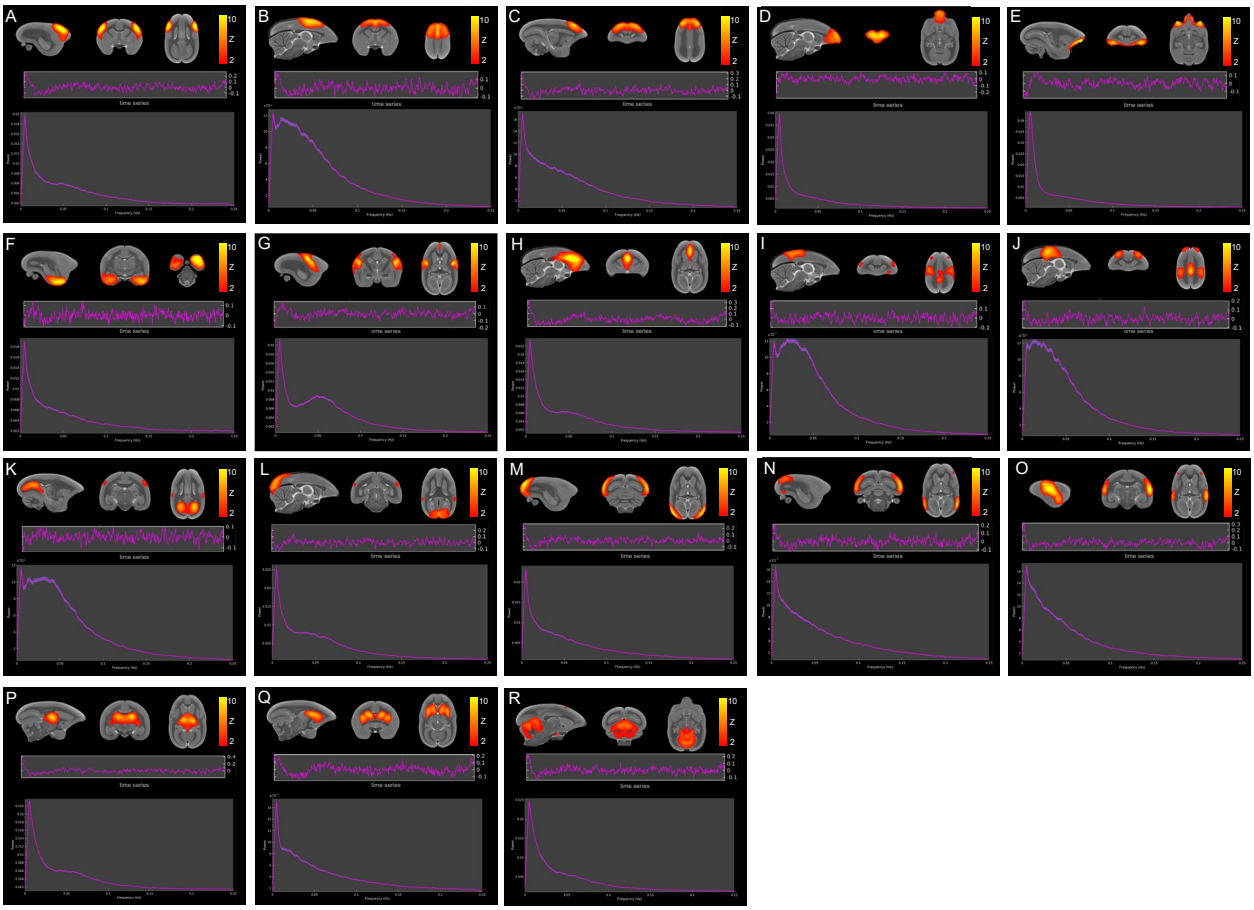

Figure S5. Similar to Figure S4 but with the time series and frequency power plotted for each component.

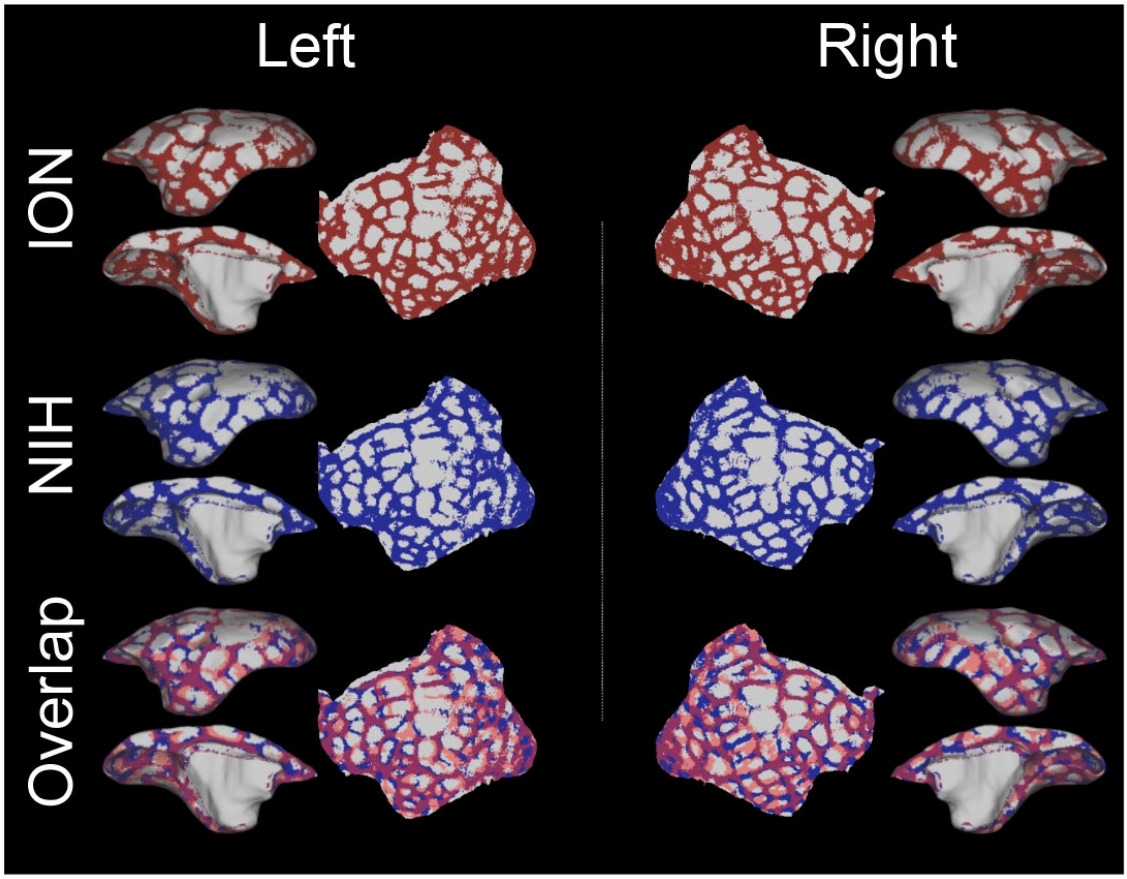

Figure S6. Boundary maps in both hemispheres from NIH and ION Dataset are highly similar. Top and middle panel: The boundary maps in both hemispheres from NIH and ION datasets after thresholding both at the 75th percentile of boundary map values. Bottom: The comparison between two boundary maps (Top and middle) in both hemispheres. Light blue: NIH boundaries; pink: ION boundaries; purple: the overlapping boundaries between datasets.

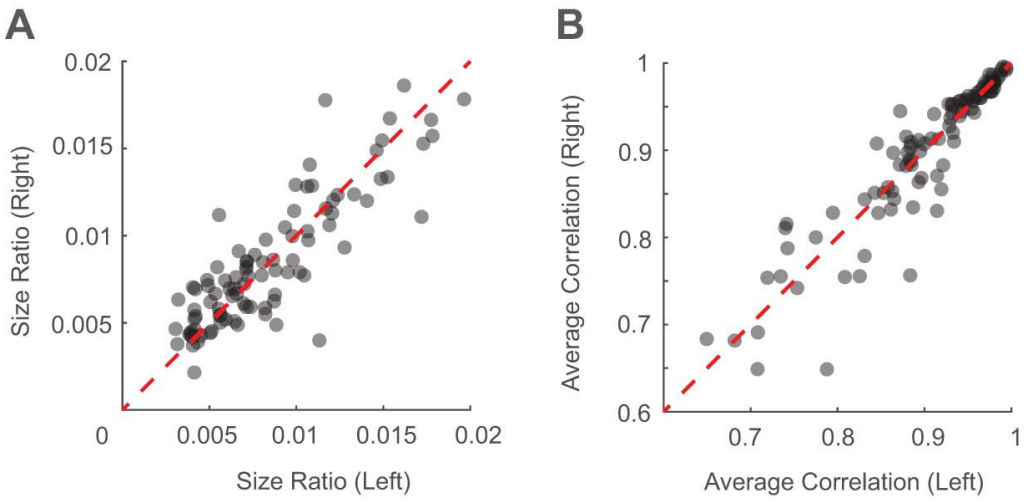

Figure S7. The functional parcels are highly similar across the hemisphere. (A) The parcel sizes. (B) The functional connectivity patterns of parcels. The dashed line represents the diagonal line.

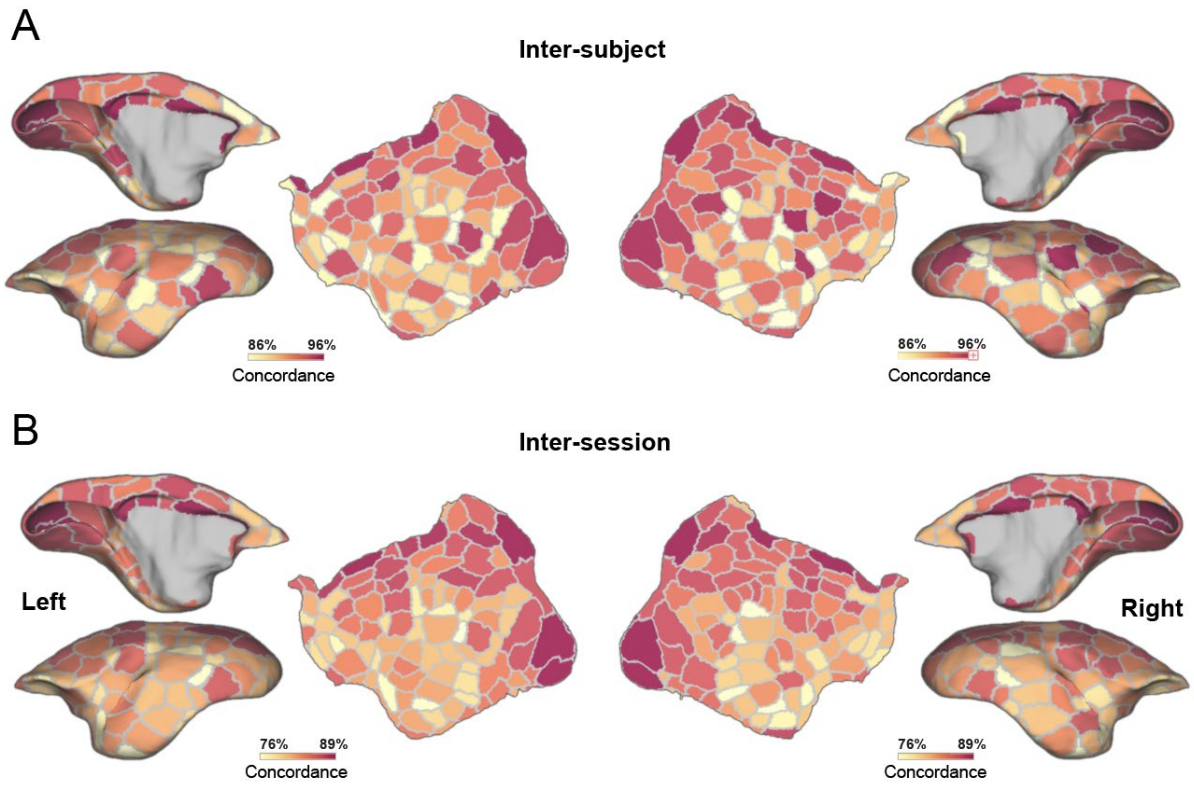

Figure S8. The variation of individual mapping parcels by the deep neural network. (A) The concordance of inter-subject parcels. (B) The concordance of inter-session parcels.

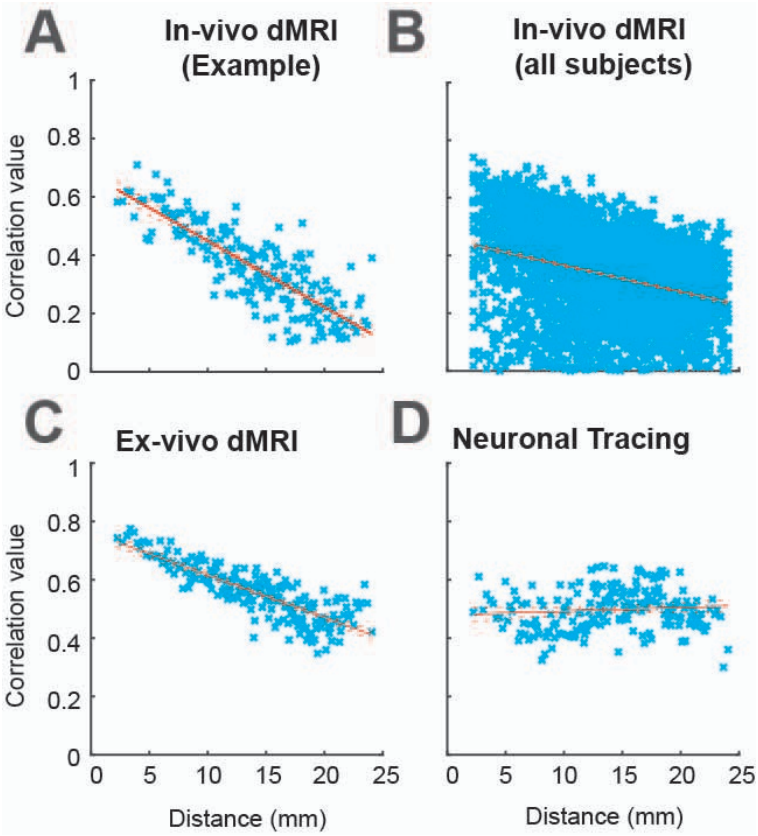

Figure S9. The simulation results in terms of the connection distance based on MBMv4. In a clockwise direction, the panels present the simulation results of the in-vivo diffusion MRI from an example subject (A), in-vivo diffusion MRI from all subjects (B), the ultra-high resolution ex-vivo diffusion MRI (C), and the neuronal-tracing dataset (D). The solid orange lines represent marginal regression lines, and dashed lines represent a 95% confidence interval.

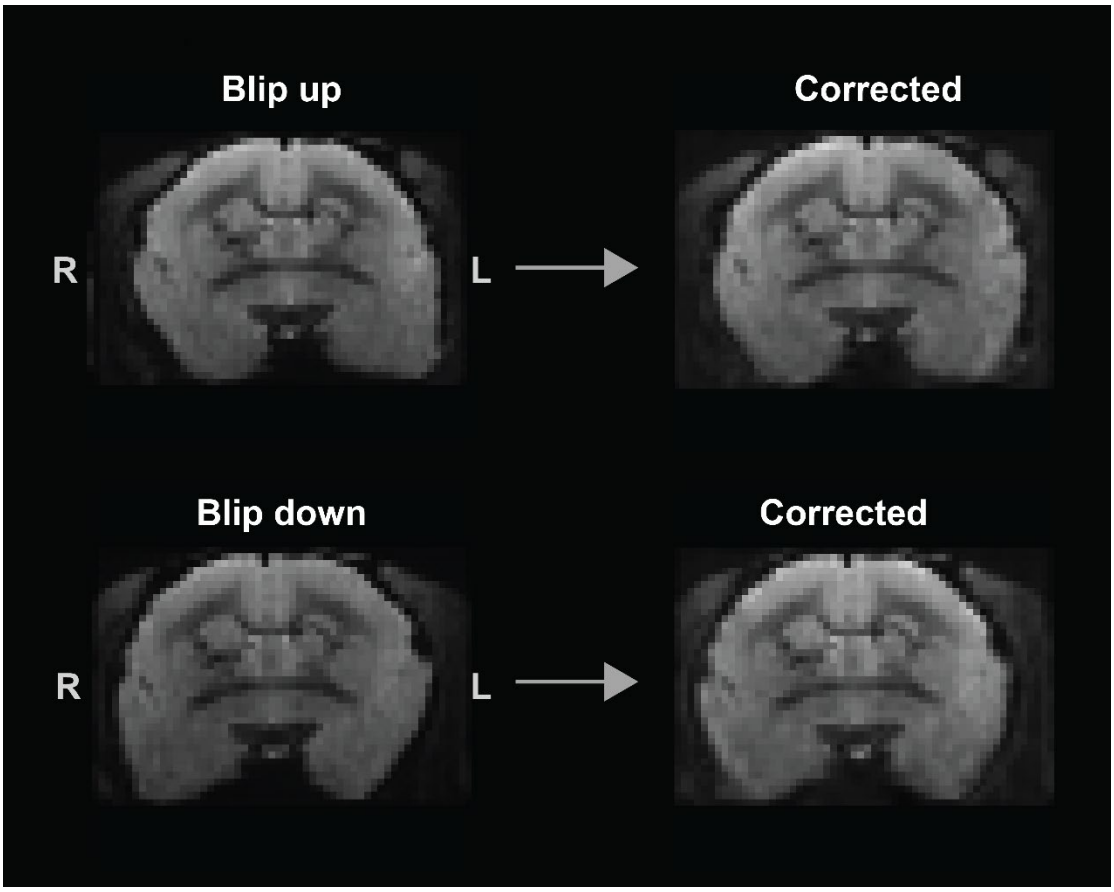

Figure S10. Examples of the top-up EPI distortion correction.

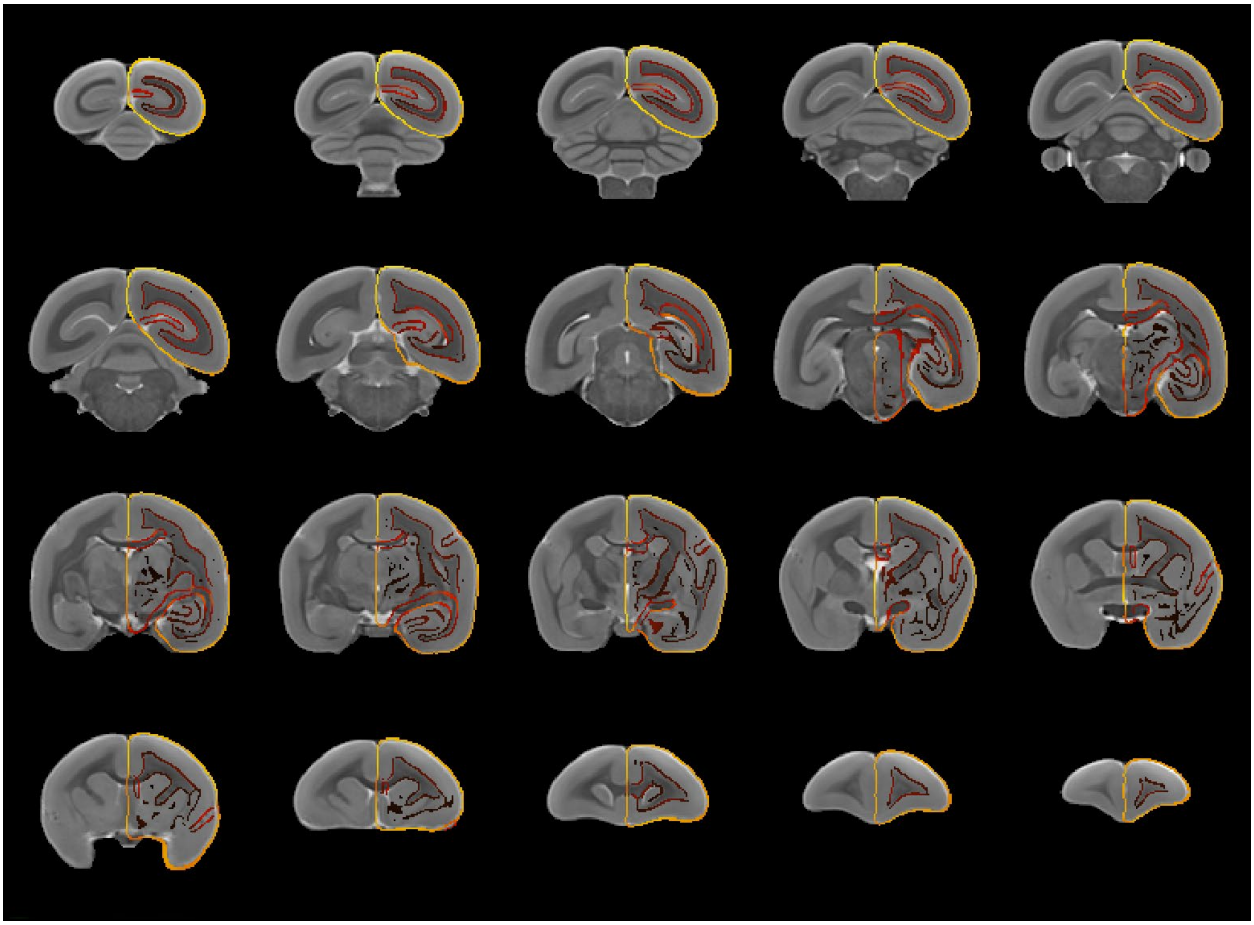

Figure S11. The registration of the histological NM template to the MBMv3 MRI template. The underlay is the T2w template of the MBMv3, and the overlay is the outline of the histological NM template that is transformed on the MBMv3 template space. The outline is generated by the @AddEdge function of the AFNI (using the default setting).

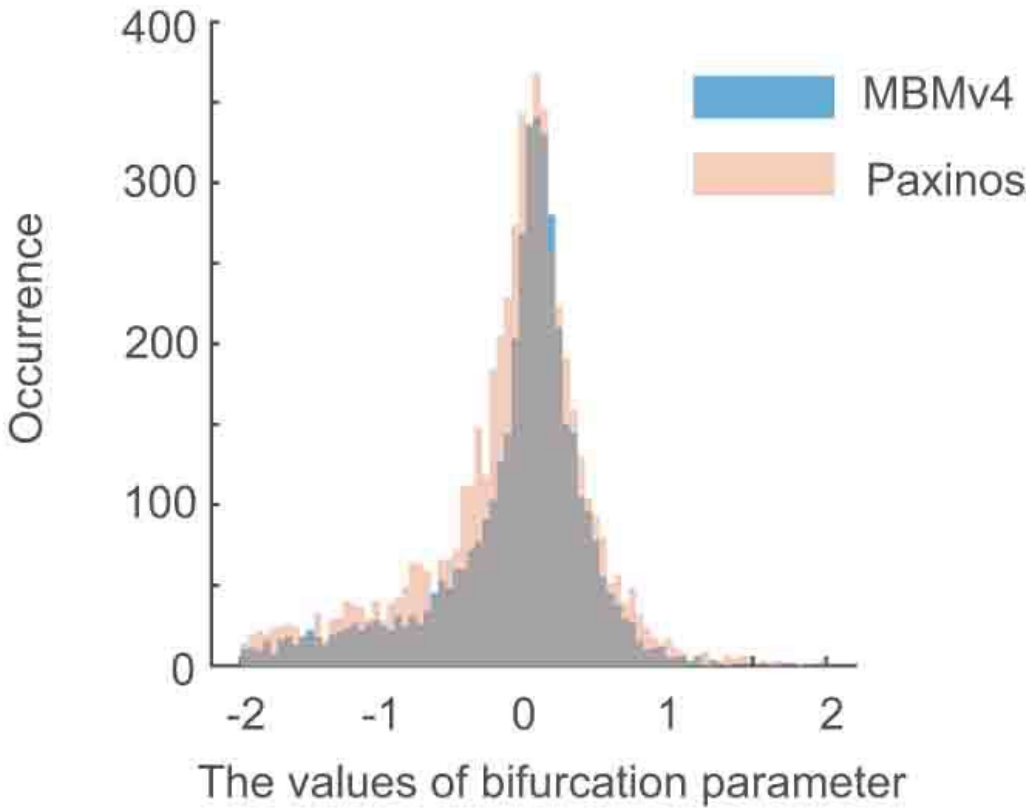

Figure S12. The distribution histogram of optimal bifurcation parameter. Blue: based on MBMv4 atlas; Light red: based on Paxinos atlas;

Table S1. The additional details of datasets. The table also included in the data release

Click to download the table:

https://1drv.ms/x/s!Ai5giu0ky8jkioVt17rGgJ91SNv9Dw?e=G29cCf

Table S2. Summary of head motion quality control for each fMRI run. The table is also included in the data release.

Click to download the table:

https://1drv.ms/x/s!Ai5giu0ky8jkioVn6KnzDItyWzqcKw?e=MTathY